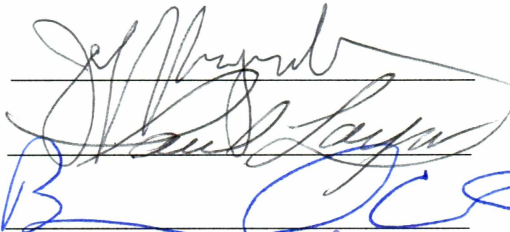


ISOSTASY AND ORIGIN OF THE  
ALPHA-MENDELEEV RIDGE, ARCTIC OCEAN

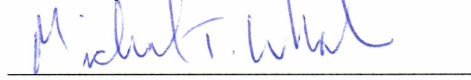
By

Christina C. Williams

RECOMMENDED:



Advisory Committee Chair

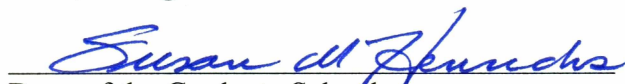


Vice Chair, Department of Geology  
& Geophysics

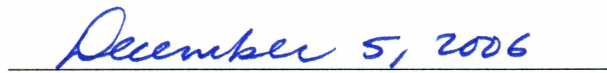
APPROVED:



Dean, College of Natural Science and Mathematics



Dean of the Graduate School



Date

ISOSTASY AND ORIGIN OF THE  
ALPHA-MENDELEEV RIDGE, ARCTIC OCEAN

A  
THESIS

Presented to the Faculty  
of the University of Alaska Fairbanks

In Partial Fulfillment of the Requirements  
for the Degree of

MASTER OF SCIENCE

By

Christina C. Williams, B.S.

Fairbanks, Alaska

December 2006

ALASKA  
QB  
331  
W55  
2006

## ABSTRACT

The Alpha-Mendeleev Ridge is an aseismic ridge bisecting the Amerasian Basin, Arctic Ocean. There is no widely accepted theory of formation. Gravity and bathymetry data from the poorly understood ridge are used to constrain the isostatic compensation of the feature in the frequency domain. Spectral analysis of the cross correlation between gravity and bathymetry along nine data transects collected from submarines and ice breakers over the ridge yield an average crustal thickness estimate of 30 km and density estimate of  $2.75 \text{ g-cm}^{-3}$ . It also suggests compensation by local isostasy, as a near-ridge oceanic plateau or an extended fragment of continental shelf. These parameters are used to constrain gravity models of crustal structure. The analysis suggests no difference between the compensation of the Alpha and Mendeleev Ridges. These results are discussed in the broader tectonic context of the Amerasian Basin, in light of the current controversy over the formation of the ridge.

## TABLE OF CONTENTS

	Page
Signature Page .....	i
Title Page .....	ii
Abstract .....	iii
Table of Contents .....	iv
List of Figures .....	v
List of Tables .....	vii
Acknowledgements.....	viii
<b>Chapter 1 Introduction .....</b>	<b>1</b>
1.1 Tectonic History of the Arctic Ocean .....	1
1.2 The Alpha-Mendeleev Ridge.....	7
1.3 Purpose.....	9
<b>Chapter 2 Spectral Analysis.....</b>	<b>11</b>
2.1 Introduction to Spectral Analysis.....	11
2.1.1 Historical Results .....	11
2.1.2 Theory .....	12
2.1.2a Calculating the Admittance.....	12
2.1.2b Theoretical Isostatic Models .....	14
2.1.3 Methods & Data Reduction .....	15
2.2 Shiptrack Data.....	16
2.3 The Alpha-Mendeleev Ridge Complex .....	20
2.3.1 Results of Spectral Analysis .....	20
2.3.2 Isostatic Models for the Alpha-Mendeleev Ridge Complex.....	24
2.4 Alpha-Mendeleev Ridge Sections.....	31
2.4.1 Results of Spectral Analysis .....	31
2.4.2 Isostatic Models for Alpha and Mendeleev Ridges .....	32

	Page
2.5 Discussion of Results.....	37
2.6 Data Grids.....	38
<b>Chapter 3 Gravity Modeling.....</b>	<b>44</b>
3.1 Introduction.....	44
3.2 Methods.....	44
3.2.1 2-D Shiptrack Models.....	44
3.3 Results.....	45
3.3.1 2-D Crustal Models.....	45
3.3.2 Grid Crustal Models.....	52
<b>Chapter 4 Discussion.....</b>	<b>56</b>
4.1 Near Spreading Center Hotspot Activity.....	57
4.2 Rifted Continental Fragment.....	60
4.3 Consistent Tectonic Models of the Amerasian Basin.....	62
<b>Chapter 5 Conclusions.....</b>	<b>64</b>
References.....	65
Appendix.....	CD

## LIST OF FIGURES

	Page
Figure 1.1: Features of the Arctic Ocean .....	2
Figure 1.2: The Arctic Canadian islands transform model .....	4
Figure 1.3: Beginning of spreading given the Arctic Alaska transform model .....	5
Figure 1.4: Rotational model for opening of the Amerasian Basin .....	6
Figure 2.1: Location of nine projected shiptracks over the AMR .....	18
Figure 2.2: Projected bathymetry (gray fill) and gravity (black line) .....	19
Figure 2.3: Bathymetry (a) and gravity (b) power spectra .....	21
Figure 2.4: Lithospheric filter, calculated by inverse FTT .....	22
Figure 2.5: Coherence as defined in text .....	22
Figure 2.6: $\text{Log}_{10}$ of the calculated admittance (blue) with linear fit (red) .....	24
Figure 2.7: Diagram showing difference between regional and local compensation .....	26
Figure 2.8a-b: admittance (red) with sets of theoretical Airy models .....	28
Figure 2.9: Observed admittance (red) with a set of theoretical flexural models .....	29
Figure 2.10: Reduced $\chi^2$ in parameter space for the Airy isostatic model .....	30
Figure 2.11: Lithospheric filters for AR (left) and MR (right) .....	32
Figure 2.12: $\text{Log}_{10}$ of the calculated admittance (blue) with linear fit (red) .....	32
Figure 2.13: Observed admittance (red) with a set of theoretical Airy models .....	33
Figure 2.14: Observed admittance (red) with a set of theoretical flexure models .....	34
Figure 2.15: Reduced $\chi^2$ in parameter space for the Airy isostatic model .....	35
Figure 2.16: Reduced $\chi^2$ in parameter space for the flexural isostatic model .....	36
Figure 2.17: Reduced $\chi^2$ in parameter space for the flexural isostatic model .....	36
Figure 2.18: Locations of 27 profiles sampled from the IBCAO and AGP .....	40
Figure 2.19: $\text{Log}_{10}$ of the calculated admittance (blue) with linear fit (red) .....	41
Figure 2.20: (a) Observed grid admittance (red) with a set of theoretical Airy .....	42
Figure 2.21: Two examples of the grid sampled gravity (line) .....	43
Figure 3.1 (A-I): Crustal models for the nine shiptracks .....	47

	Page
Figure 3.2: AGP gravity for the MR (left) and AR (right) .....	54
Figure 3.3: Predicted gravity for the MR (left) and the AR (right) .....	54
Figure 4.1: Geometry of first near-ridge hotspot model .....	58
Figure 4.2: Geometry of second near-ridge hotspot model .....	60
Figure 4.3: Geometry of AMR as rifted continental margin .....	62

### LIST OF TABLES

Table 2.1: Summary of results of best isostatic model .....	37
Table 3.1: Summary of model misfits for crustal models.....	51
Table 3.2: Summary of model misfits with average thickness .....	52

## ACKNOWLEDGEMENTS

This work would not have been possible without the help and support of my advisor, Dr. Bernard Coakley. He gave me and this study direction, and he deserves thanks for all his help, patience, and encouragement. My committee members, Dr. Jeff Freymueller and Dr. Paul Layer, were also vital to the project, especially the computational aspects. I owe the solution to many computational impasses to them. All my committee members were invaluable in advising the analysis of my work and keeping me on track.

In addition I must also thank Dr. Bill Witte, for advising me with a variety of computer difficulties, and making sure I had access to the right resources. I also owe thanks to my officemate and fellow Arctic tectonics enthusiast, Dayton Dove, whose discussions with me on the tectonics of the Amerasian Basin were important in guiding my understanding. Funding for this study was provided by the National Science Foundation, grant OPP-0241004

Finally, I owe deep gratitude to my friends and family, for their support. In particular, my parents have always been an inexhaustible resource of support and encouragement.



## **1. INTRODUCTION**

The Arctic Ocean (figure 1.1) is the last frontier of marine geophysics. The primary reasons are that data acquisition is difficult due to permanent cover of sea ice, and the unique tectonics of the smallest ocean basin. With such restricted access to the ocean floor, the amount of information about the crustal structure we can gather is very limited. In such a difficult environment, various geophysical data, such as gravity and bathymetry, have an advantage as they can be measured easily from the surface. It is possible, however, to model crustal structure based on these geophysical data, and draw conclusions about the formation of oceanic features and try to understand the tectonic history. This study employs gravity and bathymetry data to constrain the origin of the Alpha-Mendeleev Ridge, based on modeled crustal structure. Some knowledge of the crustal structure can provide us with insight into the history of the Arctic Ocean seafloor.

### **1.1 Tectonic History of the Arctic Ocean**

Of the two main basins of the Arctic Ocean, which are each of distinct age, the Eurasian Basin has a better known history. The Eurasian basin was opened by seafloor spreading of the Mid-Atlantic Ridge north across the Arctic (Coakley and Cochran, 1998). This rifting severed the Lomonosov Ridge from the Barents Shelf (Jackson and Johnson, 1986). Spreading has continued since rifting at around 56 Ma (Brozena et al., 2003), at ultra-slow spreading rates ranging between 0.6 and 1.3 cm/year (Coakley and Cochran, 1998).

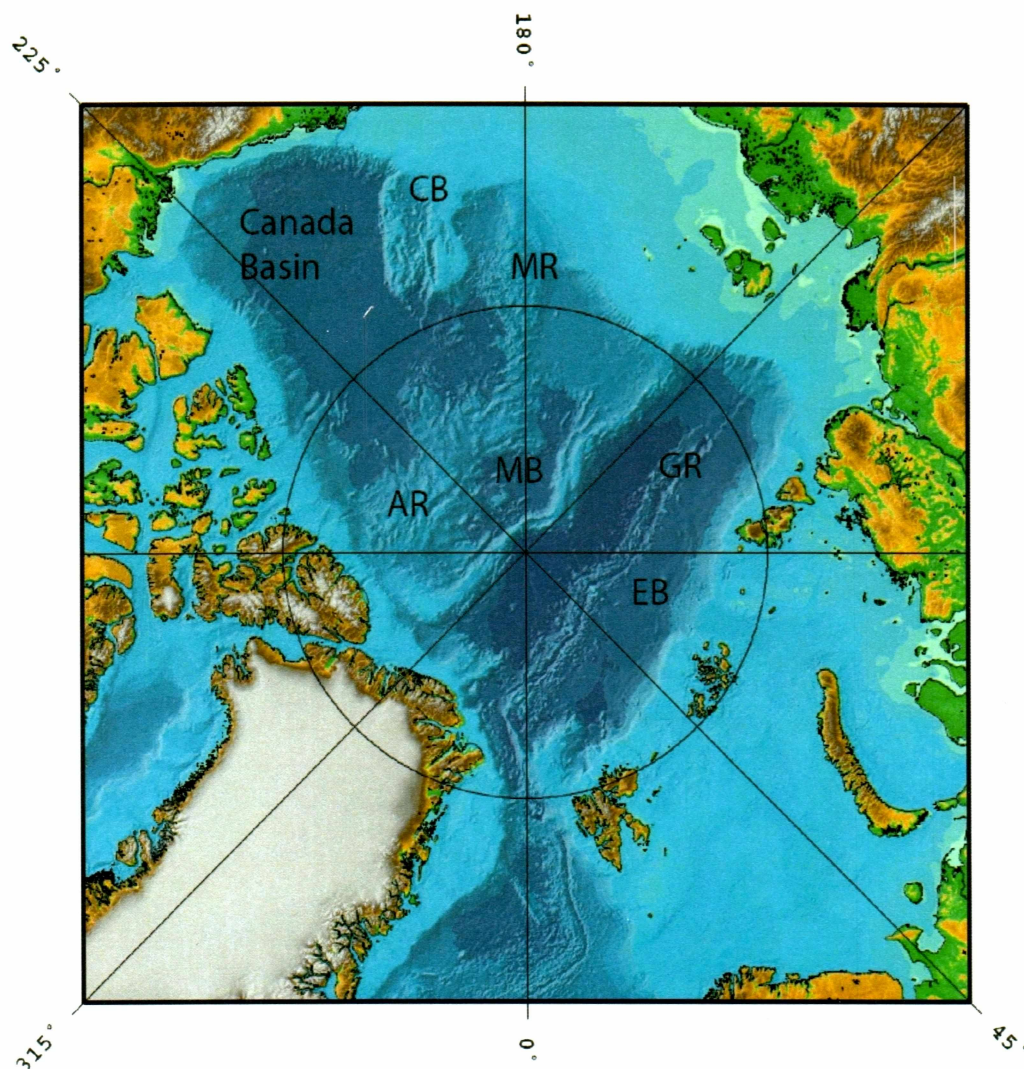


Figure 1.1: Features of the Arctic Ocean. Source data is from the International Bathymetric Chart of the Arctic Ocean (Jakobsson et al., 2000), discussed in section 2.5. Labeled features are the Chukchi Borderland (CB), Alpha Ridge (AR), Mendeleev Ridge (MR), Lomonosov Ridge (LR), and Gakkel Ridge (GR). Labeled basins are the Eurasian Basin (EB), Makarov Basin (MB), and the Canada Basin. The Makarov Basin and Canada Basin together make up the Amerasian Basin.

The opening of the Amerasian Basin, which is made up of the Canada and Makarov Basins, is not well constrained because of, in part, the lack of distinct, symmetric linear magnetic anomalies that are the signature of seafloor spreading (Vogt et al., 1982). There is evidence that the Amerasian Basin contains oceanic crust which is Mesozoic in age, but we know little of its structure and seismic data are sparse (Jokat,

2003). The lack of any obvious plate boundaries in the Amerasian Basin makes reconstructing the history of the basin difficult. In addition it is home to the most enigmatic bathymetric features in the Arctic, including the Chukchi Plateau, Northwind Ridge, and the Alpha-Mendeleev Ridge (AMR). The Chukchi Plateau and Northwind Ridge together comprise the Chukchi Borderland, and are thought to be stretched continental crust which originated in the North Chukchi Basin or the continental shelf adjacent to Banks Island in arctic Canada (Lawver and Scotese, 1990). The origin of the AMR is currently under debate. The unknown nature of the features in this basin further complicates the reconstruction of this basin. A conclusive theory of the Mesozoic evolution of the Amerasian Basin still remains to be found, not for the lack of interest, but rather for the lack of data and testable hypotheses.

One of the first hypotheses for the origin described the Canada Basin as oceanized continental crust that subsided due to root erosion caused by mantle convection (Belousov, 1970). This has been abandoned since evidence now exists that suggests the Amerasian Basin is composed of oceanic crust (Jackson et al., 1995; Jokat, 2003). There are currently four proposed tectonic theories for the opening of an oceanic Amerasian Basin.

The captured oceanic plate model suggests that the oceanic crust of the Canada Basin was originally part of the Kula Plate which was formed in the Pacific during the Early Mesozoic, and subsequently isolated into the Arctic during the mid-Cretaceous (Lawver and Scotese, 1990), however magnetic anomaly maps fail to resolve seafloor spreading anomalies associated with this.

The first seafloor spreading theory listed here is known as the “Arctic Islands Transform” model, shown in figure 1.2. It requires seafloor spreading in the Amerasian Basin along a ridge axis parallel to the Lomonosov Ridge, presumably the AMR. A consequence of this theory is that the Canadian Arctic margin must be a transform fault,

and Arctic Alaska is a passive margin which rifted from Eurasia (Crane, 1987; Lawver and Scotese, 1990). Coastal geologic evidence such as extensional faults suggests Arctic Alaska is in fact a passive margin (Grantz et al., 1990), however the deep structure of the Canadian Arctic is unknown. The presence of the Chukchi Borderland off the Siberian Shelf presents complications for this model as it is difficult to see how it could exist with a transform fault there.

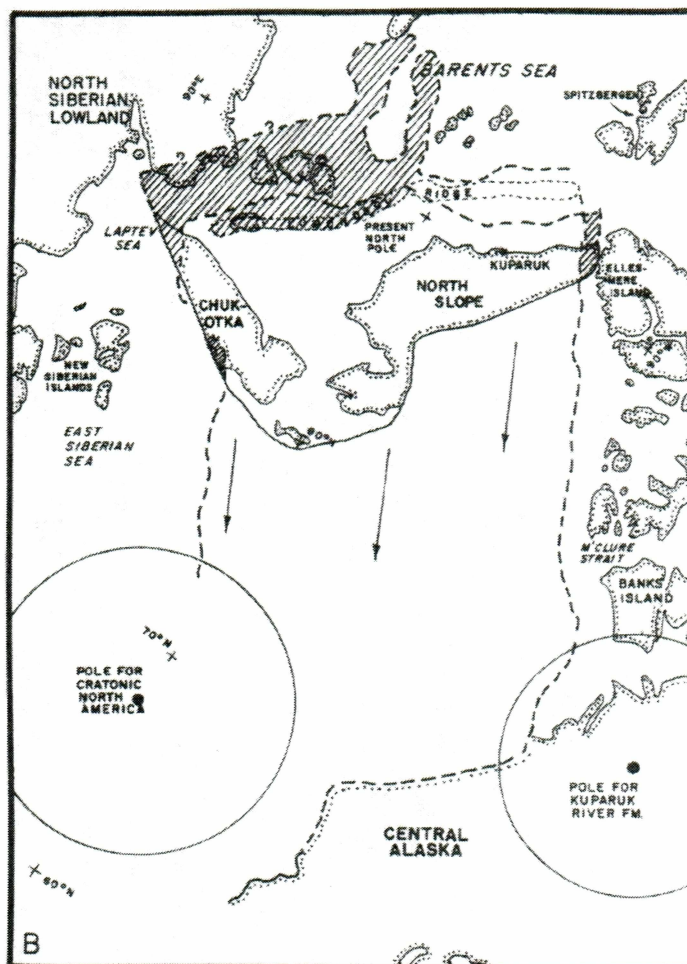


Figure 1.2: The Arctic Canadian islands transform model, taken from Halgedahl and Jarrard (1987). Arrows show motion of Alaska-Chukotka microplate towards central Alaska as it rifts from the Barents Shelf.

A second translational model is the “Arctic Alaska transform”, shown in figure 1.3, where the spreading axis in the Canada Basin is perpendicular to the Lomonosov Ridge, so that the Lomonosov Ridge and Arctic Alaskan shelf are transform faults and Arctic Canadian and East Siberian shelves are rifted margins (Vogt et al., 1982; Lane, 1997). The presence of the Chukchi Borderland is more consistent with this model; however there is no evidence of a transform motion along the Alaskan shelf. The existence of a transform fault on the Amerasian side of the Lomonosov Ridge has not been shown, but has been inferred (Cochran et al., 2005).

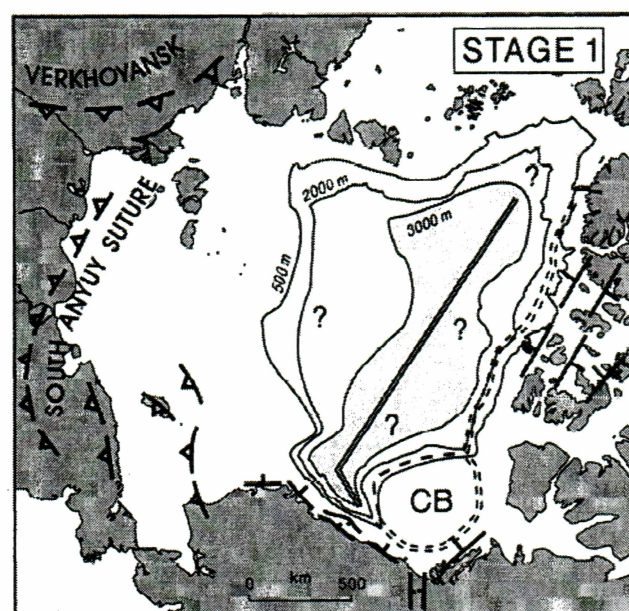


Figure 1.3: Beginning of spreading given the Arctic Alaska transform model, figure from Lane (1997). Spreading center given by solid double line, and a second stage of spreading at a later time is given by dashed line. Reconstructed position of the Chukchi Borderland given by CB.

The last seafloor spreading theory is the rotational model, shown in figure 1.4. Geologic similarities between Arctic Alaska and Chukotka and Arctic Canada have led to the popular theory that Arctic Alaska and Russia were once attached to Arctic Canada. The Amerasian Basin formed when the Alaska-Chukotka microplate rifted from Arctic Canada and rotated approximately 66 degrees about a pole in the Mackenzie Delta area

(Embry and Dixon, 1994). Evidence includes paleomagnetic data (Halgedahl and Jarrard, 1987), similar stratigraphy and evidence of sutured continental crust (Embry and Dixon, 1994). Potential field data in the Canada Basin resolves what resembles a fan shaped series of linear magnetic anomalies that could account for 35 degrees of rotation (Lane, 1997). In addition, stratigraphic data from the Chukchi Borderland suggests that it was also once connected to the Arctic Canadian and Alaskan margins, and thus is evidence supporting the rotational opening of the Canada Basin (Grantz et al., 1998).

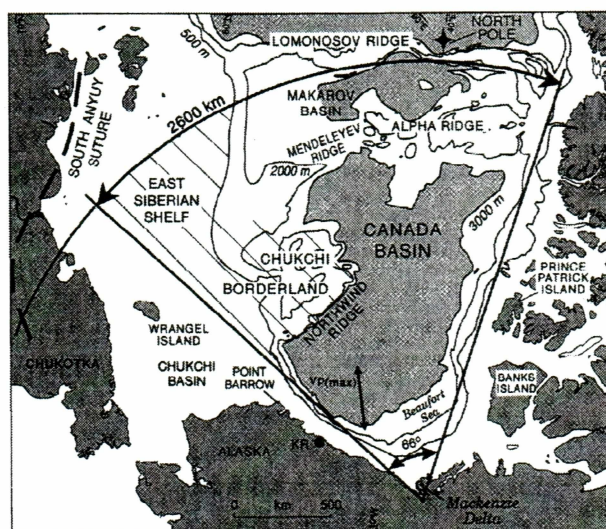


Figure 1.4: Rotational model for opening of the Amerasian Basin, as published by Lane (1997). Hypothesized transform fault at the Lomonosov Ridge indicated by curved arrows.

While there is evidence in favor of the rotation theory, it has its share of unsupportive data, including that conclusive anomalies associated with seafloor spreading have not been discovered. New evidence from sedimentary rocks in Chukotka now suggest that its sedimentary history is completely unrelated to that of Arctic Canada and Eastern Alaska and instead must have originated close to the Russian shelf (Miller et al., 2006). Rotational opening of basins have been seen elsewhere on the earth, such as the Bay of Biscay (Taylor et al., 1981), but no rotational analog of similar scale has been found. The existence of the Chukchi Borderland (as well as the Mendeleev Ridge (MR) if it is pre-Cretaceous in age) in its present location also conflicts with the full 66 degrees of

rotation by seafloor spreading (Lane, 1997). The lack of evidence of a transform fault on the Canada Basin side of the AMR or the Amerasian Basin side of the Lomonosov Ridge is an additional hurdle for the rotational theory (Lane, 1997). The details of the geometry and chronology of the rotational spreading are also unresolved, as different theories have nonlinear spreading and transform faults with separate periods of active spreading (Lawver and Scotese, 1990). But since the AMR crosses the Amerasian Basin the nature of the ridge complex as a whole is important for any formation theory of the Canada Basin.

## **1.2 The Alpha-Mendeleev Ridge**

In the past, theories of the opening of the Canada Basin have explained the AMR as being formed through all the varied processes that create or modify the seafloor. The presence of a bathymetric discontinuity, Cooperation Gap, has allowed for the suggestion that the two ridges are in fact separate features. Prior to the ice station T-3 mission, Alpha Ridge (AR) was thought to be non-volcanic and continental in origin (Hall, 1970). Vogt and Ostenso (1970) theorized that the AMR is an extinct spreading center, a theory which was consistent with the results from station T-3 (Hall, 1970) and various geophysical data presented in Hall (1973). A summit graben and fractures resembling transform faults and offsets, like those found on the Mid-Atlantic Ridge, observed on the AR were thought to be evidence of seafloor spreading. This idea was rejected by both Herron et al. (1974) and DeLaurier (1978) because the AMR did not exhibit symmetric magnetic anomalies, and was bathymetrically too high to have been a spreading center in the Late Cretaceous according to the age-depth relationship which determines thermal subsidence of oceanic lithosphere (Delaurier, 1978).

Kerr (1983) tried to resolve this issue by inferring a continental fragment underlying the ridge, which prevented it from subsiding. It was instead suggested that the AMR was a subduction zone formed between 81-63 Ma after the formation of the Canada Basin by compression due to seafloor spreading at the Gakkel Ridge (Herron et al.,

1974). This theory was later refuted by geochemical data from the Canadian Expedition to Study the Alpha Ridge (CESAR) which showed that the AR consists of alkalic basalts which are not typical of island arcs (Von Wagoner et al., 1986).

Prior to the CESAR mission, the AR was interpreted as a hotspot track (Vogt et al., 1979). Later supported by the CESAR data, the theory of the AMR advanced with the suggestion that it was formed by the hotspot, currently beneath Iceland, passing through the Amerasian Basin (Lawver and Muller, 1994) while seafloor spreading in the Canada Basin rotated Arctic Alaska and Russia from the North American Plate (Jackson and Johnson, 1986). Later evidence indicated that the AMR might be better explained as a record of hotspot activity near a spreading center, similar to the Iceland-Faeroe Ridge (Weber, 1990). The AMR has even been hypothesized as a hybrid feature in which the MR and non-linear central AR were originally a joined linear submarine plateau that split when the western AR was formed by seafloor spreading that divided the two ridges (Lane, 1997). This hypothesis allowed for explanation of the kink in the AMR that mimics the Lomonosov Ridge. The rest of the eastern AR then formed as a track of the Icelandic hotspot (Lane, 1997). Most recently however, the suggestion has been made that the AMR is extended continental crust rifted from the Barents shelf before the rifting of the Lomonosov Ridge (Miller et al., 2006).

While the geophysical data must be honored by any workable theory, geological sampling of the AMR offers other constraints. Dredging of the AR crest during the CESAR mission returned samples of sediment and basement which provided some age constraints and compositions. Several seismic surveys revealed a sediment layer 500-1000 meters thick on the eastern and central AR (Forsyth et al., 1986a; Jokat, 2003). In dredged samples, various fossil deposits were found which constrain the time of deposition to be Late Cretaceous (Von Wagoner et al., 1986). The oldest sediments were of late Campanian to Maastrichtian age (84-66 Ma) so the AR must have been formed before then (Von Wagoner et al., 1986). The dredged bedrock sample collected by the



CESAR mission from the AR crest was found to be alkalic mafic basalt, which is indicative of midplate volcanism (Von Wagoner et al., 1986). Petrological and geochemical work indicates the sample was erupted in shallow water. It is thought the volcanic rocks from the AR are the precursors to the basaltic lavas that were erupted from the Iceland Hotspot onto Ellesmere Island in Arctic Canada (Lawver and Muller, 1994), which have been dated to 105-92 Ma (Embry and Osadetz, 1988; Tarduno et al., 1998). The results of the seismic refraction studies show a crust-mantle boundary at 38 km below the ridge crest, and suggest that the crustal structure of the AR is similar to that of other oceanic plateaus (Von Wagoner et al., 1986).

As for the MR, there is very little known other than bathymetry and sparse observations of gravity and magnetic anomalies. It is known, however, that Russian dredging has returned Paleozoic fossils in limestone, suggesting the MR is continental in origin (unpublished data from presentation by Kaban'kov et al., given in St Petersburg, 2003). Seismic surveys over the ridge have suggested a depth to the Moho of 32 km beneath the ridge crest (Lebedeva-Ivanova et al., 2006). A recent seismic survey over the MR from the 2005 cruise of the USCG Icebreaker Healy suggests that there is an average sediment thickness of 600 meters (Dove et al., 2006). The question of the origin and evolution of the AMR as two separate features or as one is still unanswered.

### **1.3 Purpose**

This study employs gravity and bathymetry data to constrain the origins of the AR and the MR. The data consists of both individual shiptracks and profiles sampled from gridded datasets across the ridges. The shiptrack data were collected during a series of nuclear submarine cruises in the Arctic as part of the SCience ICe EXercise (SCICEX; Edwards and Coakley, 2003). The gridded data sources are the International Bathymetric Chart of the Arctic Ocean (IBCAO, Jakobsson et al., 2000, at <http://www.ngdc.noaa.gov/mgg/bathymetry/arctic/arctic.html>) and the Arctic Gravity Project (AGP, at <http://earth-info.nga.mil/GandG/wgs84/agp/index.html>). The data are

subject to two analyses: first, spectral methods are used to correlate gravity and bathymetry, and the results are fit to theoretical isostatic models. Using the constraints provided by bathymetry and gravity, mechanism of compensation, average crustal thickness, and density were estimated. Second, using these constraints from the frequency analysis, the ridges were modeled to constrain density structures and test the isostatic model. Any differences or similarities between ridge regions will be discussed in geologic context of formation and its relevance to the various tectonic models in the Canada Basin.

## 2. SPECTRAL ANALYSIS

### 2.1 Introduction to Spectral Analysis

#### 2.1.1 Historical Results

Inferring crustal structure from potential field anomalies has a long history (e.g., Blakely, 1996). Most of the power in gravity anomalies over oceanic ridges, especially the shorter wavelength features, are due to the bathymetry. Bathymetry is the largest density contrast, and is the closest to the point of observation. Gravity anomaly data also contain information about density changes within the lithosphere, the mechanism of compensation, and the depth of the crust-mantle boundary. To probe these characteristics, a quantitative study of isostasy and crustal properties can be done using spectral analysis of gravity and bathymetry. Because spectral analysis quantifies the wavelength dependence of the correlation between datasets, it can be applied to oceanic ridges to associate gravity anomaly features with their source contributions.

In the oceans, bathymetry is a load that engages an isostatic response. The response causes changes in the depth to the Moho, and redistributes the upper mantle to maintain hydrostatic equilibrium. This mass redistribution, being deeper and typically broader than the surface load, has a longer wavelength influence on the observed gravity. The wavelength of this response is proportional to the strength of the lithosphere. By examining how bathymetry and gravity are correlated in the frequency domain, spectral analysis can constrain the isostatic compensation of oceanic features. Previous studies have also provided evidence of the tectonic environment in which oceanic features were formed. Watts (1978) analyzed the Hawaii-Emperor island chain and found that the islands are best described by regionally compensated loads on a rigid lithospheric plate. It was also observed that the best fitting elastic thickness of the lithosphere changed along the island chain axis. This evidence is consistent with the theory that strength of the

oceanic lithosphere under seamounts correlates with the age difference between the seamount and age of the underlying oceanic crust (Watts, 1978).

Similarly, the analysis of Detrick and Watts (1979) over the eastern and western Walvis Ridge showed that the ridge sections are compensated differently. The eastern Walvis Ridge exhibited Airy isostasy and is consistent with the theory that it was formed by hotspot volcanism on young lithosphere near a spreading center. In contrast, the mechanism of compensation of the western Walvis ridge was best described by a flexural model which implied that the ridge was superimposed on older stronger lithosphere. These findings are consistent with the theory that the eastern ridge was formed by near-ridge hotspot volcanism but, after a movement of the hotspot away from the spreading center, the western ridge formed on older stronger lithosphere (Detrick and Watts, 1979). It was also shown that the Ninetyeast Ridge in the Indian Ocean was entirely locally compensated, consistent with the theory that the entire ridge was formed by near-ridge volcanism. Spectral methods will similarly shed light on the tectonic environment in which parts of the AMR formed.

## **2.1.2 Theory**

### **2.1.2a Calculating the Admittance**

Compensation of a mass load cannot be observed directly, as it is hidden by mass distributions due to geologic processes such as sedimentation. It is easier instead to use gravity anomalies which are directly observable and are sensitive to both topographic load and flexure of the lithosphere (Watts, 2001). This allows the observed gravity profile  $g(x)$  to be written as a function of flexure  $y(x)$ , which represents the compensating load.

The method treats the lithosphere as a filter, or system with an input and output, which relates bathymetry and the compensation due to bathymetric loading. This can be done by modeling the lithosphere as an elastic plate on a viscous mantle and calculating the system's isostatic response to loading (Watts, 2001). Mathematically, the load is

treated as a set of impulses to the system. With knowledge of the observed bathymetry (load) and gravity response, it is possible to estimate the lithospheric filter. Its isostatic response can then be estimated quantitatively as deformation or flexure of the lithospheric plate. The compensation  $y(x)$  can be compared to predicted responses for isostatic mechanisms such as Airy, Pratt, or flexural isostasy. Linear filter theory allows us to write the observed gravity  $g(x)$  as the convolution of the lithospheric filter and the topographic load (in the oceanic case, the bathymetry  $b(x)$ ), and is given by the equation

$$g = z \otimes b = \int_{-\infty}^{\infty} z(x') b(x - x') dx' \quad (1)$$

where the cross indicates the convolution operation,  $z(x)$  is the set of filter coefficients, and  $x'$  is the variable of integration. The lithospheric filter is a linear space-invariant filter so that the principle of superposition holds for all topographic loads and their superimposed elastic flexural responses.

As convolution is a complicated and inefficient computational process, using Fourier transforms and working in the wavenumber domain results in a simpler, faster calculation. The Fourier transform is an integral transform applied to a function  $f(x)$  in the spatial domain and results in a function of wavenumber given by

$$F(k) = \int_{-\infty}^{\infty} f(x) e^{ikx} dx \quad (2)$$

where wavenumber  $k = 2\pi/\lambda$ . Working in the wavenumber domain is supported by the convolution theorem which states that for a spatial time series, convolution in the spatial domain becomes simple multiplication in the wavenumber domain (Arfken and Weber, 2001). In the wavenumber domain, the convolution integral now becomes

$$G(k) = Z(k) B(k) \quad (3)$$

where upper case functions are the Fourier transforms of the corresponding lower case functions. The filter in the wavenumber domain,  $Z(k)$ , is now called the gravitational admittance, and is the Fourier transform of the filter coefficients  $z(x)$ . Since both the

gravity and bathymetry functions are directly observable they can be used to calculate the gravitational admittance

$$Z(k) = G(k)/B(k) \quad (4)$$

where  $Z(k)$  is a description of the relationship between gravity and bathymetry over the ridge, which is dependent on the state of isostasy. Because it contains isostatic information and is independent of any isostatic model it can be used to fit the observations to theoretical isostatic models.

### 2.1.2b Theoretical Isostatic Models

$Z(k)$  for a given isostatic model is easily calculated for a given topography and compensating mass, according to models such as Airy and Pratt isostasy, as well as plate models in which loads are regionally compensated by elastic flexure of lithosphere beneath the topographic load (Watts, 2001). Fitting the observed admittance to the theoretical isostatic models constrains the possible mechanisms of compensation, as well as crustal thickness and average density of the ridge. The models are calculated by making use of Fourier methods (Parker, 1972) for calculating gravity anomalies due to arbitrary layers of mass. The gravity anomalies caused by these arbitrary layers are difficult to evaluate using line integral techniques but by working in the wavenumber domain their computation is much easier (Parker, 1972). Specific models have been computed for Airy and flexural models of isostasy for the studies over the Hawaii-Emperor Seamount Chain, the Mid-Atlantic, Walvis and Ninetyeast Ridges (Watts, 1978; Detrick and Watts, 1979; Cochran, 1979).

The theoretical admittances are calculated from gravity and bathymetry as summarized by Watts (2001). It was shown by Parker (1972) that in the wavenumber domain, to first approximation, the gravity anomaly, indicated by  $\Delta G'(k)$  to differentiate it from the gravitational constant  $G$ , due to an arbitrary density interface measured a distance  $d$  above a density interface is given by

$$\Delta G'(k) = 2\pi G \Delta \rho e^{-kd} H(k) \quad (5)$$

where  $H(k)$  is the Fourier transform of the elevation across a density interface and  $\Delta\rho$  is the density contrast across this interface. If the ridge bathymetry is used as  $H(k)$  and  $\Delta\rho$  is the density contrast between bathymetry and seawater, this function describes the gravity anomaly due simply to the topography over the ridge. Since the admittance function is given by equation 3, and we have defined  $H(k) = B(k)$ , the admittance for uncompensated topography becomes:

$$Z(k) = 2\pi G \Delta\rho e^{-kd} \quad (6)$$

Independent anomalies due to individual sources can be superimposed, so additional contributions to the overall gravity field may be found using the same method and added to the topographic contribution. Different mechanisms of compensation will be considered as additional contributions. Specific models tested in this study will be presented with the data analysis.

### 2.1.3 Methods and Data Reduction

The methods of data reduction are taken from the series of studies “Isostasy in the World’s Oceans 1-3” (Watts, 1978; Cochran, 1979; Detrick and Watts, 1979), and are summarized here. For this study the continuous functions are represented by discrete sets of observed data points, and the Fourier transform integral can then be written as a sum

$$F(k) = \frac{1}{N} \sum_{x=0}^{N-1} f(x) e^{-ikx/N} \quad (7)$$

(Arfken and Weber, 2001). Spectral analysis for this study requires that each discrete gravity and bathymetry dataset is treated as a time series for the purpose of Fourier transformation and the related admittance and isostatic response function calculations. For each profile this includes data resampling at evenly spaced points, subtraction of the mean and trend, tapering using a Tukey cosine window for continuity purposes, and finally buffering each dataset with zeros (Watts, 1978). The computation of the discrete Fourier transforms are done using the fast Fourier transform (FFT) algorithm of Cooley and Tukey (1965), which is the discrete Fourier transform calculated for datasets of size  $N$  where  $N$  is a power of two. The use of fast Fourier transforms for  $N$  a power of two

greatly decreases the number of computations required from  $N^2$  to  $N \log N$  (Cooley and Tukey, 1965) and thus increases time efficiency of the calculation. The final treated datasets are each 2048 points, a power of 2, to maximize the efficiency of the FFT algorithm.

Due to considerable noise that is introduced during the FFT of the data, several smoothing techniques are used to maximize the signal. It has been shown that in the presence of noise, instead of using equation 3, an estimate with greater signal to noise ratio can be found by first calculating the cross spectrum and bathymetric power spectrum such that

$$Z(k) = \frac{G(k)B^*(k)}{B(k)B^*(k)} \quad (8)$$

where \* denotes complex conjugate (McKenzie and Bowin, 1976). To estimate overall admittance of the ridge, the cross spectra and bathymetry power were stacked separately before estimating admittance. All data manipulation and calculations were done in Matlab, with the exception of the data sampling which was done with Generic Mapping Tools (GMT; Wessel and Smith, 1991). Scripts are presented in Appendix 1.

## 2.2 Shiptrack Data

The analysis was done for two separate pairs of datasets over the AMR. It was first done using individual projected shiptracks collected during the Science Ice Exercise (SCICEX) missions between 1993 and 1999. The SCICEX program was a series of cruises to the Arctic Ocean to collect geophysical, biological and oceanographic data using U.S. Navy nuclear submarines (Edwards and Coakley, 2003). Shiptrack data over the AMR include four shiptracks from the 1995 cruise of US Navy submarine Cavalla, three shiptracks from the 1996 cruise of the USS Pogy, one shiptrack from each the 1997 USS Archerfish cruise and the 1999 USS Hawkbill cruise. The analysis was also done for the gridded bathymetry and gravity and will be described in section 2.6.



In total six shiptracks cross the AR and three cross the MR. Gravity data from all the cruises were obtained using a Bell BGM-3 gravimeter. Bathymetry was measured using the narrow-beam high resolution fathometer AN/BQN-17 (Edwards and Coakley, 2003). Data from the shiptracks on the map in figure 2.1 are presented in figure 2.2.

Spectral analysis requires data perpendicular to ridge axis, so when necessary shiptracks were projected perpendicular to the ridge using GMT. The projection operation is a rescaling of shiptracks in distance, such that the measurements become evenly spaced and linear, and are oriented perpendicular to the ridge axis. The projected shiptracks were sampled every one kilometer, as spectral analysis requires evenly spaced datapoints. It is clear from the shiptrack data that the gravity mimics the bathymetry over long wavelengths, so bathymetry must contribute to most of the gravity power for long wavelengths (Watts, 1978). In the following sections the analysis and results from the shiptrack data are presented for the AMR as a whole, and the AR and MR as separate oceanic features.

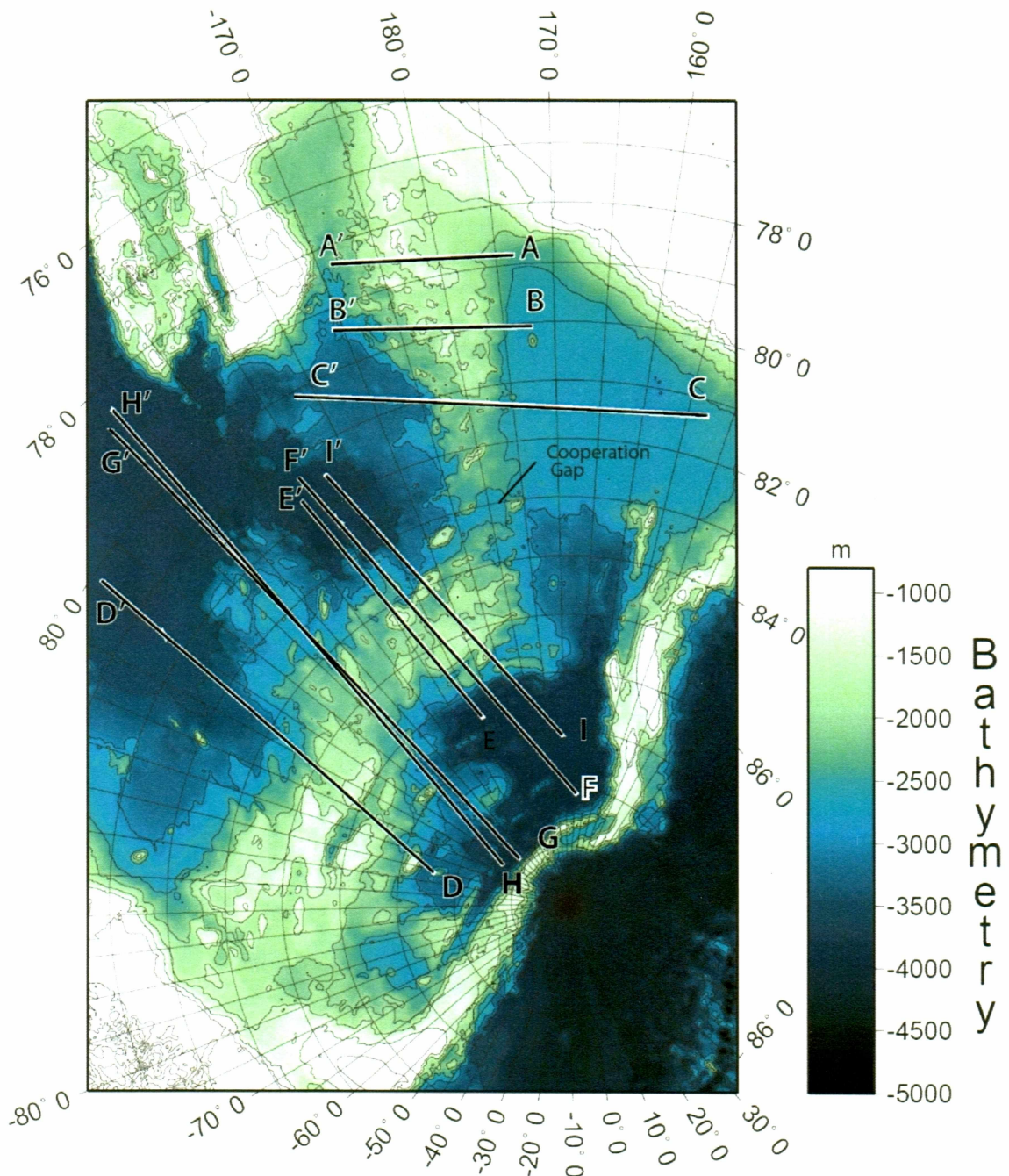


Figure 2.1: Location of nine projected shiptracks over the AMR used in the spectral analysis. Map source, Jakobsson et al. (2000). Shiptrack sources: shiptracks A-C, H from Cavalla 1995, D-F from Pogy 1996, G from Archerfish 1997, I from Hawkbill 1999. Cooperation gap, the bathymetric discontinuity which divides Alpha and Mendeleev Ridges, is labeled. From this definition profiles A-C are on Mendeleev Ridge and D-I are on Alpha Ridge.

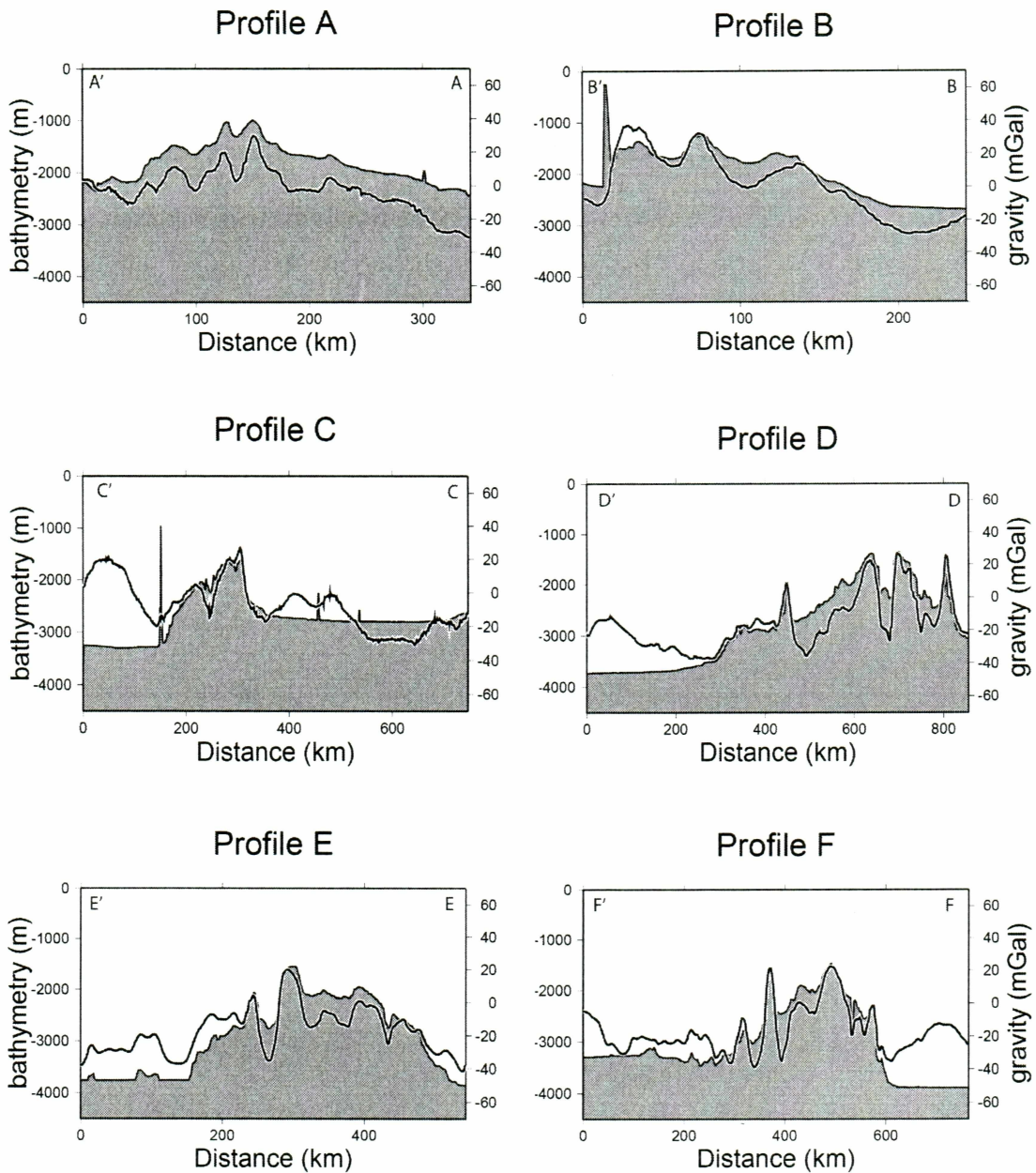


Figure 2.2: Projected bathymetry (gray fill) and gravity (black line) data from nine shiptracks, labeled A-I. Profile endpoints are labeled as in figure 2.1.

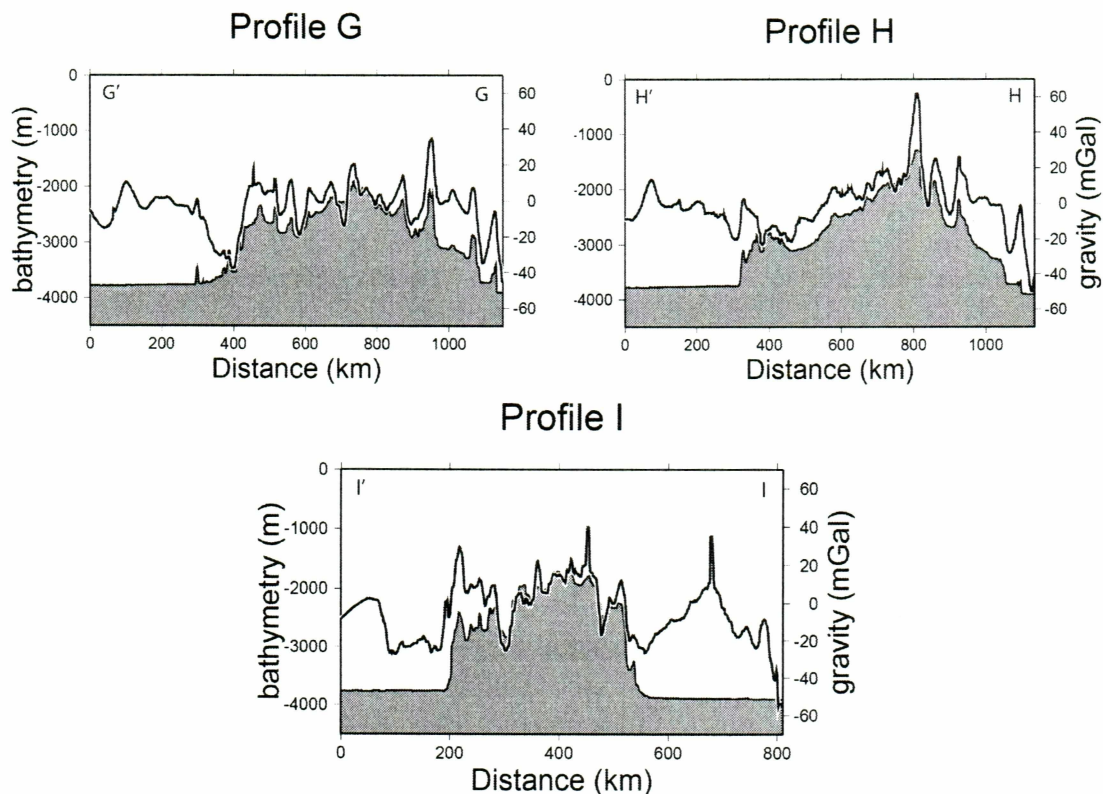


Figure 2.2 Continued: Projected bathymetry (gray fill) and gravity (black line) data from nine shiptracks, labeled A-I. Profile endpoints are labeled as in figure 2.1

## 2.3 The Alpha-Mendelev Ridge Complex

### 2.3.1 Results of Spectral Analysis

This section describes the results from the entire set of nine shiptracks to analyze the entire AMR as one oceanic feature, and follow the methods of Watts (1978). The stacking of all shiptracks diminishes any signal unique to the Alpha or Mendeleev ridge section, which will be analyzed separately in the next section. The stacked gravity and bathymetry power spectra are defined as

$$P_{bath}(k) = B(k)B^*(k) / N \quad (9a)$$

$$P_{grav}(k) = G(k)G^*(k) / N \quad (9b)$$

where capital B and G indicate the Fourier transform of the bathymetry and gravity datasets, \* indicates the complex conjugate, and N is the total number of points in the

dataset. These power spectra are an average of the contribution from each shiptrack, shown in figure 2.3. The bathymetry spectrum and cross spectrum are used to compute the overall gravitational admittance from equation 2, as discussed in the previous section. Calculating the inverse Fourier transform of the admittance gives the filter, shown in figure 2.4. The filter is an impulse response function that describes the gravity effect of a line load given by the topography (Watts, 1978). The high central peak indicates high correlation between gravity and topography, and the negative side lobes indicate anti-correlation, and are the effects of isostatic compensation (Watts, 1978). Coherence between the datasets quantifies how the bathymetry correlates with the observed gravity field, and is given by:

$$\gamma^2 = \frac{N}{N-1} \left[ \frac{G(k)B^*(k)}{P_{bath}(k)P_{grav}(k)} - 1 \right] \quad (10)$$

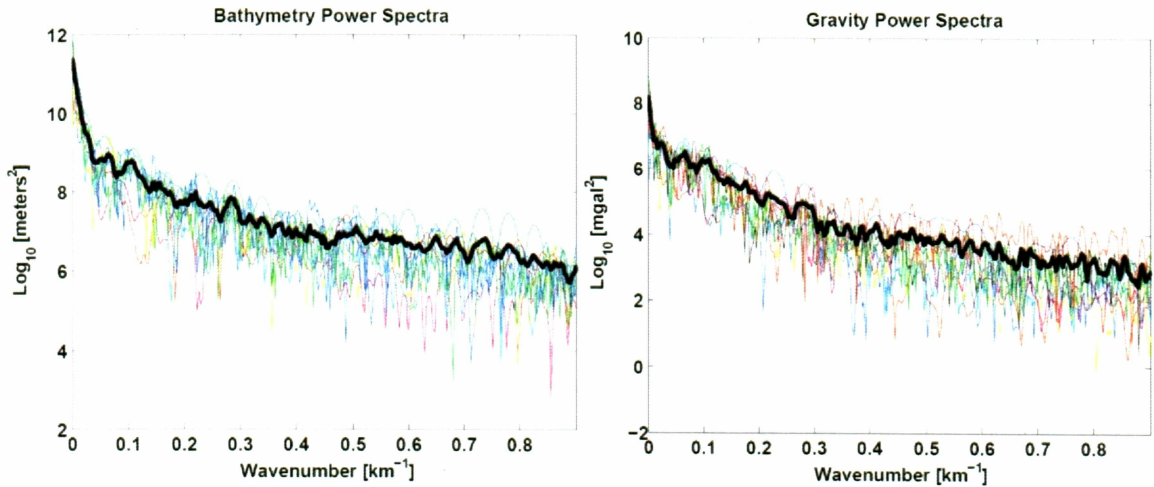


Figure 2.3: Bathymetry (a) and gravity (b) power spectra as defined in text. Power spectra for each individual shiptrack is plotted in color beneath the stacked power spectra in thick black. Power spectra represent the distribution of gravity and bathymetry energy present in the profiles.

As shown in figure 2.5, the coherence is low at the very smallest wavenumbers but in general is high for slightly larger wavenumbers, between  $0.008 < k < 0.6 \text{ km}^{-1}$ , indicating that for these wavelengths gravity is primarily due to bathymetry, not compensation. The admittance function drops off to zero at very long wavelengths, reflecting isostatic

compensation (Watts, 2001). This wavenumber region where coherence is high in the observed admittance is thus due to the gravity signal from uncompensated topography.

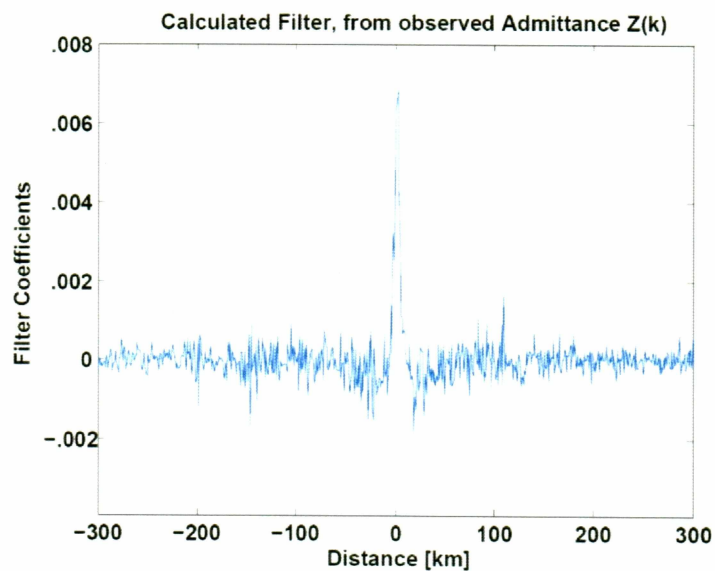


Figure 2.4: Lithospheric filter, calculated by inverse FFT from gravitation admittance into the spatial domain. The central 600 km about the ridge axis is plotted here.

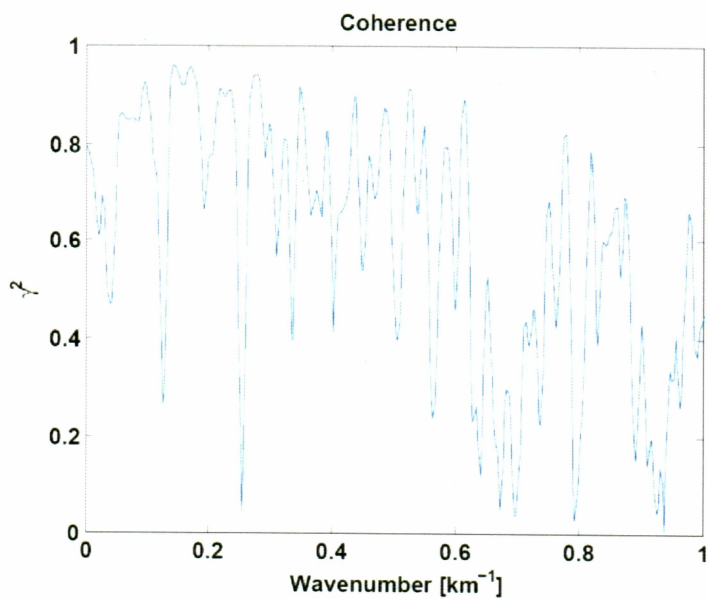


Figure 2.5: Coherence as defined in text.

The observed admittance is presented in figure 2.6. The theoretical admittance for uncompensated topography was derived in section 2.1.2b,

$$Z(k) = 2\pi G(\rho_c - \rho_w)e^{-kd} \quad (11)$$

where  $G$  is the gravitational constant,  $\rho_c$  is density of topography,  $\rho_w$  is density of seawater and  $d$  is the mean water depth. Taking the  $\log_{10}$  of both sides returns

$$\log_{10} Z(k) = -kd \log_{10} e + \log_{10}[2\pi G(\rho_c - \rho_w)] \quad (12)$$

a function linear in  $k$ . A linear fit to the observed admittance in the wavenumber range where uncompensated topography is significant is also shown in figure 2.6. The fit gives an estimate of average water depth as 2.26 km and 2.51 g-cm<sup>-3</sup>, which compares well with the actual value of average water depth, 2.78 km. The estimated average density of the topography of 2.51 g-cm<sup>-3</sup> is not unreasonable for sediments, which have been found on the surface of the AMR, but is a little low for alkalic mafic basalt that is the basement rock dredged from the AR crest (Von Wagoner et al., 1986). The linear fit, however, is unacceptable for wavenumbers  $k < 0.008 \text{ km}^{-1}$  indicating significant compensation to the bathymetry.

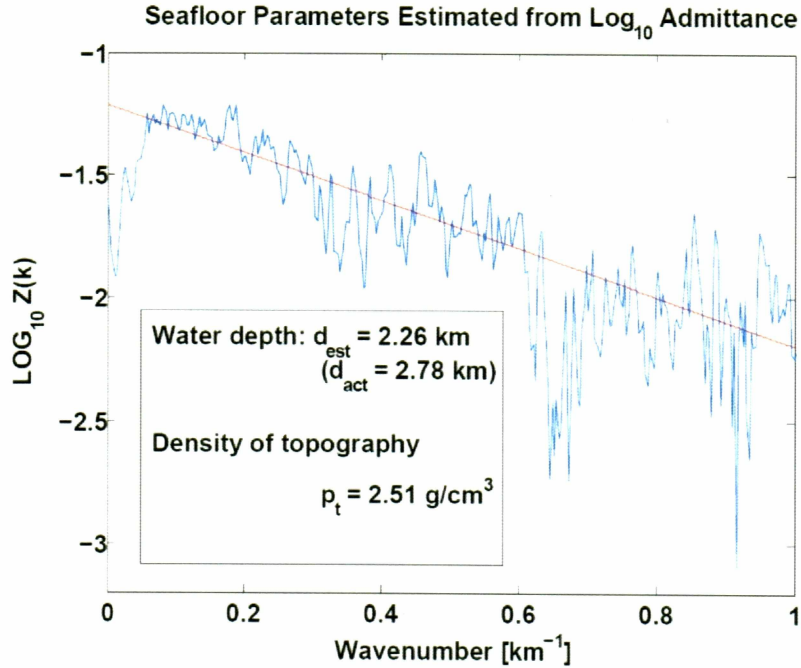


Figure 2.6: Log<sub>10</sub> of the calculated admittance (blue) with linear fit (red) between  $0.008 < k < 0.6 \text{ km}^{-1}$ . Water depth and crustal density estimated from the fit compare well with actual and realistic values as shown in the table and described above.

### 2.3.2 Isostatic Models for the Alpha-Mendelev Ridge Complex

It is possible to compare the calculated admittance with analytically derived admittance functions that describe possible states of isostasy. As mentioned in section 2.1.2b, for a mechanism of compensation, the theoretical  $Z_{\text{model}}(k)$  is given by  $Z_{\text{model}}(k) = G_{\text{model}}(k) / H(k)$  where  $G_{\text{model}}(k) = G_{\text{topo}}(k) + G_{\text{comp}}(k)$ . It was shown that the admittance due only to seafloor topography, measured at sea level is given by equation 5,  $Z(k) = 2\pi G(\rho_c - \rho_w)e^{-kd}$ . Thus the theoretical  $Z(k)$  is independent of bathymetry and can be used to fit the observed admittance to a specific isostatic mechanism. Two of the possible isostatic mechanisms for oceanic crust, derived in Watts (2001), are summarized here.

Airy isostasy posits that a topographic high is supported by thicker crust. The lower density crust ‘floats’ on the denser mantle. The increased thickness can be



determined using Archimedes Principle, and it can be shown that the thickness of the root is related to the thickness of the topography according to

$$T_{root} = T_{topo} \frac{\rho_c - \rho_w}{\rho_m - \rho_c} \quad (13)$$

assuming constant density with depth (Watts, 2001). Therefore two density interfaces contribute to the overall gravity signal in the model,

$$\Delta G_{total}(k) = \Delta G_{topo}(k) + \Delta G_{root}(k) \quad (14)$$

Gravity anomaly due to topography  $\Delta G_{topo}(k)$  is defined in section 2.1.2b. Gravity anomaly due to the root  $\Delta G_{root}(k)$  can be found by taking advantage of the root's thickness dependence on the bathymetric height for a column of mass. For the root-mantle interface, depth to the interface becomes  $d + t$  where  $d$  is still seafloor depth and  $t$  is total crustal thickness under that column. The interface is now defined as the root  $R(k)$  which as mentioned earlier is related to the topography by

$$R(k) = -H(k) \frac{\rho_c - \rho_w}{\rho_m - \rho_c} \quad (15)$$

By the same methods the gravity anomaly due to the compensation is

$$\Delta G_{comp}(k) = 2\pi G(\rho_c - \rho_w)R(k)e^{-k(d+t)} \quad (16)$$

so that

$$\Delta G_{total}(k) = 2\pi G(\rho_c - \rho_w)H(k)[e^{-kd} - e^{-k(d+t)}] \quad (17)$$

and

$$Z(k) = 2\pi G(\rho_c - \rho_w)e^{-kd}(1 - e^{-kt}) \quad (18)$$

This is the theoretical admittance for the Airy isostasy case, where average crustal density  $\rho_c$  and average thickness  $t_{avg}$  are unknown, or in the case of this study, estimated from the observed admittance.

Flexural isostasy is a regional isostatic model in the sense that the stress due to a topographic load is transmitted regionally by a strong plate which supports the load. The dimensions of the distortion of the lithosphere are scaled by the strength of the

lithosphere. Stronger lithosphere will distribute the weight of the load over a broader region, whereas weaker lithosphere will not support the weight. The gravity anomaly due to the flexure,  $\Delta G_{flex}(k)$ , is derived in the same way as the Airy case, except we use the Fourier transform of the flexural displacement,  $Y(k)$ , in place of the Fourier transform of the root topography,  $R(k)$ . The Fourier transform of the flexural displacement is

$$Y(k) = -H(k) \frac{\rho_c - \rho_w}{\rho_m - \rho_c} \Phi(k) \quad (19)$$

where

$$\Phi(k) = \left[ \frac{Dk^4}{g(\rho_m - \rho_c)} + 1 \right]^{-1} \quad (20)$$

and  $D$  is the flexural rigidity and  $g$  is the acceleration due to gravity. As flexural rigidity decreases,  $\Phi(k)$  goes to one, and the flexural model converges on the Airy case where loads are compensated only locally. This can be seen by substitution of zero for  $D$ . Lithosphere with zero strength is in fact the Airy case. In the case where  $D$  is very large,  $\Phi(k)$  goes to zero, and represents the uncompensated case. Theoretical admittance for the flexural case becomes

$$Z(k) = 2\pi G(\rho_c - \rho_w) e^{-kd} [1 - e^{-kt} \Phi(k)] \quad (21)$$

In addition to average crustal density and average thickness, flexural rigidity is a free parameter and can be used to test the strength of the lithosphere. The difference between local and regional compensation can be seen in figure 2.7.

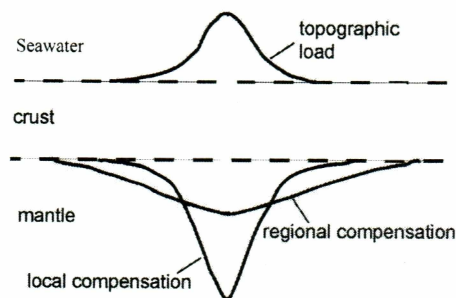


Figure 2.7: Diagram showing difference between regional and local compensation, adapted from <http://www.geophysik.uni-kiel.de/~hajjo/Bratislava/Files/Isostat/Isostat.html>

As stated in section 2.1.2b, isostatic compensation is most important at the very longest wavelengths, so the calculated admittance is compared with the isostatic models in the wavenumber range  $0 < k < 0.2 \text{ km}^{-1}$ , following common practice in the literature. A comprehensive range of model parameters are compared with the data to select the range of best fitting parameters that describe the isostasy of the AMR. Goodness of fit is quantified using the reduced  $\chi^2$  for an arbitrary function, based on the regular  $\chi^2$  goodness of fit (Bevington, 1992). Reduced  $\chi^2$  is defined as

$$\chi^2 = \frac{1}{\nu} \sum_{i=1}^N \frac{[Z^{model}(k_i) - Z^{obs}(k_i)]^2}{\sigma(k_i)} \quad (22)$$

where  $Z^{model}$  and  $Z^{obs}$  are compared at  $N$  discrete wavenumbers,  $k_i$ .  $\sigma(k)$  is the standard deviation at each wavenumber, and  $\nu$  is the number of degrees of freedom defined as  $\nu = [\text{number of points (k) used in fit}] - [\text{number of free parameters in fitting function}]$ . The standard deviation is found by making use of variations in each independent estimate of the admittance of the ridge from each independent shiptrack at each wavenumber, and is defined as

$$\sigma(k) = \sqrt{\sum_{i=1}^N [Z_i^{obs}(k)^2 - Z_{total}^{obs}(k)^2]} \quad (23)$$

where  $N$  is the number of profiles used in the stacking process. Using the reduced  $\chi^2$  ensures the value is independent of both the number of points used to fit the model and the number of free parameters in the model so that quality of fit can be compared between different models. Best fitting models have a reduced  $\chi^2$  close to one.

The observed admittance is plotted with a range of isostatic models to show sensitivity to certain parameters in figures 2.8 and 2.9. Results from both isostatic models indicate an average crustal density of  $2.8 \text{ g-cm}^{-3}$  and average crustal thickness of 20-25 km, which is consistent with findings of the CESAR mission, as well as other large igneous plateaus of oceanic origin (Von Wagoner et al., 1986). While the noise is too high to confidently determine the specific values of the parameters, it is still possible to

discriminate between mechanisms of compensation. The reduced  $\chi^2$  for the flexural model of 1.60 is slightly lower than the reduced  $\chi^2$  of 1.74 for Airy model, indicating a better fit. However the difference is small, and upon closer evaluation, the best flexural rigidity is around  $10^{20}$  Nm which indicates a young age of emplacement. And in fact the effective elastic thickness corresponding to this strength is only  $T_{\text{eff}} = 2.24$  km, as compared with the value found over the Hawaii-Emperor seamount chain of  $T_{\text{eff}} = 20\text{-}30$  km, which is known to have formed on old high strength oceanic crust. With such a low strength for the oceanic crust found over the AMR, the best flexural isostatic model is very similar to the Airy case.

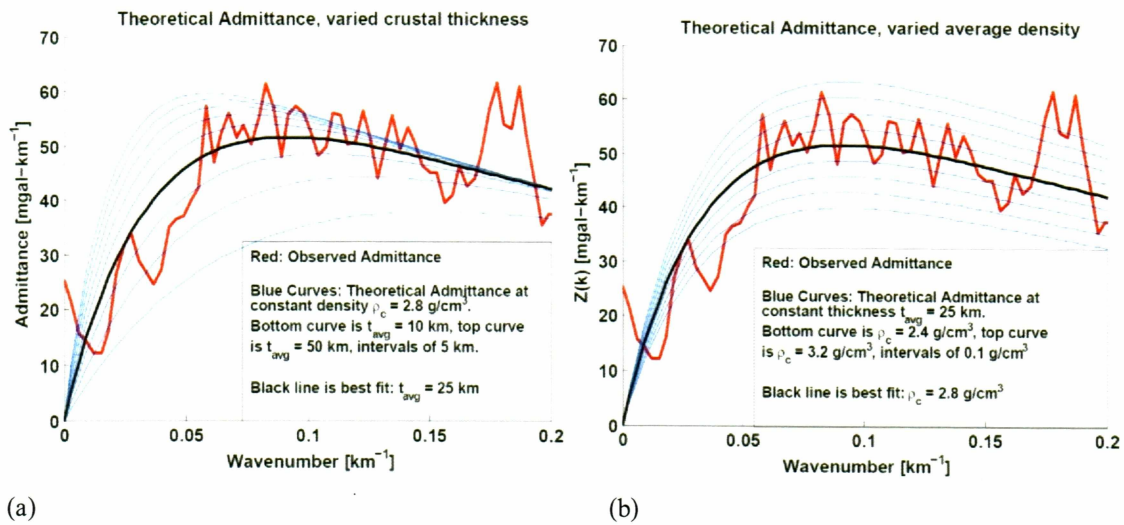


Figure 2.8a-b: Observed admittance (red) with sets of theoretical Airy models (blue). (a) Models at constant density  $\rho_c = 2.8 \text{ g-cm}^{-3}$  and average crustal thickness is varied from 10 to 50 km at intervals of 5 km. (b) Models at constant thickness  $t_{\text{avg}} = 25 \text{ km}$  and density varied from 2.4 to 3.2  $\text{g-cm}^{-3}$  with intervals of 0.1  $\text{g-cm}^{-3}$ .

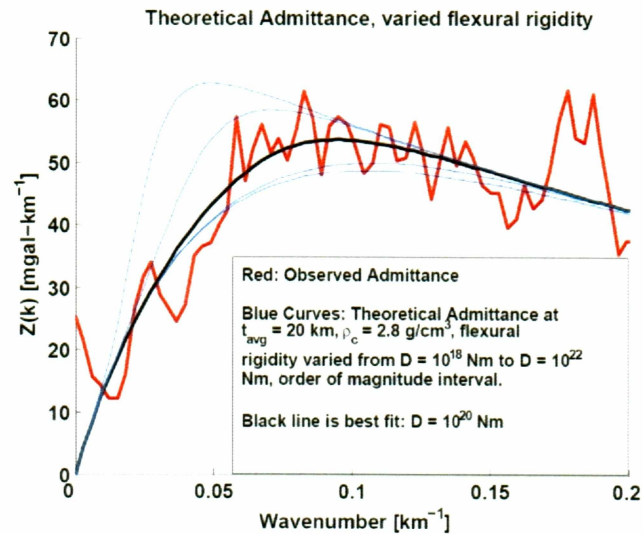


Figure 2.9: Observed admittance (red) with a set of theoretical flexural models (blue) at constant density  $\rho_c = 2.8 \text{ g-cm}^{-3}$  and constant thickness  $t_{\text{avg}} = 20 \text{ km}$ , with varying flexural rigidity from  $10^{19}$  to  $10^{22} \text{ Nm}$  with order of magnitude intervals.

The range of best fitting parameters for the Airy and flexural models are plotted in parameter space in figure 2.10. Because there are three free parameters in the flexural model the parameter space is plotted for the three best fitting flexural rigidities. Due to the noise in the admittance, only a range of parameters can be identified rather than a definitive best fit model, although the best fit according to the reduced  $\chi^2$  is marked on the plots.

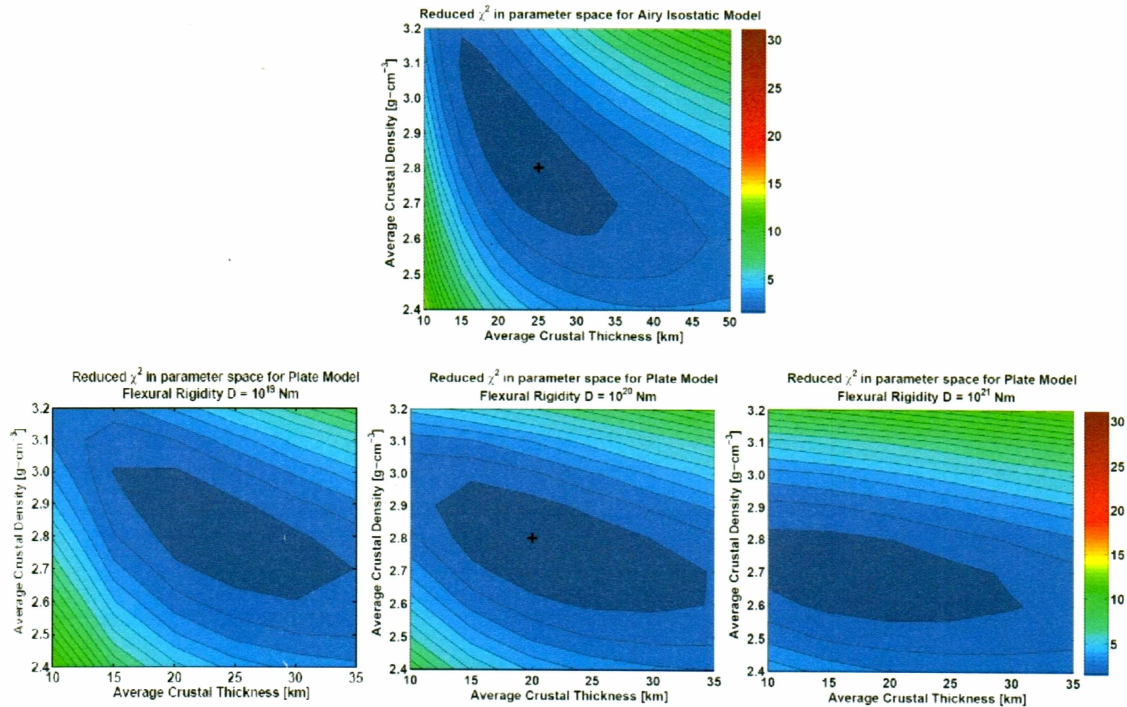


Figure 2.10: Reduced  $\chi^2$  in parameter space for the Airy isostatic model (top) and flexural isostatic model (bottom three). Average crustal thickness is plotted vs. average crustal density for four strengths (including  $D = 0$  for the Airy case) to show how  $t_{\text{avg}}$  vs.  $\rho_c$  changes with flexural rigidity. Each plot can be considered a section through a density-thickness-strength cube in parameter space. The cross shows the location of the best fit models. For the Airy case it is at  $t_{\text{avg}} = 25$  km,  $\rho_c = 2.8$  g·cm $^{-3}$  which returns a reduced  $\chi^2 = 1.74$ . The best fitting flexural rigidity is shown bottom center with an order of magnitude change in flexural rigidity shown in the right and left. The cross in center shows the location of the best fit model, with reduced  $\chi^2 = 1.60$  at  $t_{\text{avg}} = 20$  km,  $\rho_c = 2.8$  g·cm $^{-3}$  and  $D = 10^{20}$  Nm, corresponding to an effective elastic thickness  $T_{\text{eff}} = 2.24$  km, which is low for ordinary oceanic crust.

With these results a few conclusions can be drawn about the overall state of the AMR as a whole. The overall isostasy of the ridge is interpreted to be best fit by a local isostatic mechanism which is within a physically reasonable range of densities and thicknesses and is consistent with previous studies of the AR's crustal structure (Von Wagoner et al., 1986). First, this suggests if the ridge is a result of hotspot volcanism it must have formed on weak (young) lithosphere consistent with a near-spreading center volcanic hotspot. It should be noted however that extremely wide ridge features do not have large differential loading, such as that over the Hawaii-Emperor seamount chain, and may appear to be locally compensated. So, it is possible that this ridge is simply too wide for flexural effects to be observed here. An alternative suggestion, consistent with

the tectonic theory of Miller et al. (2006), is that the AMR may be extended continental shelf material that rifted from the Barents shelf prior to the opening of the Eurasian Basin. Extension in the lithosphere is a source of crustal weakness and could be responsible for the local compensation indicated here. The tectonic conclusions will be discussed in more detail in light of the complete results in the Discussion.

## **2.4 Alpha and Mendeleev Ridge sections**

### **2.4.1 Results of Spectral Analysis**

Analyzing the AR and MR as separate features permits evaluation of the mechanisms of compensation. If different mechanisms are observed, different origins should be considered for each ridge, which will have implications for the formation of the Amerasian Basin. The physiographic division between ridges is defined as Cooperation Gap, mapped in figure 2.1, which is approximately co-linear with the edge of the Canada and Makarov basins. By this definition, profiles A-C cross the MR and profiles D-I cross the AR in figures 2.1 and 2.2.

As in section 2.3.1, the results of spectral analysis are shown here for each ridge section. Filters for the AR and the MR are presented in figure 2.11. The admittances for both the AR and the MR are presented in figure 2.12. For the AR, the variability in the stacked admittance is lower due to the stacking of six profiles. For the MR, the three profiles may not have been enough to reduce the noise and reveal an isostatic signal, although it should be noted that only three profiles were used to analyze the isostasy over the Mid-Atlantic Ridge (McKenzie and Bowin, 1976). Both linear fits underestimate the average depth over the profiles and return similar estimates of density of topography. This similarity in density should be expected as the estimated density is that of the bathymetry and both ridges are known to be covered in sediments.

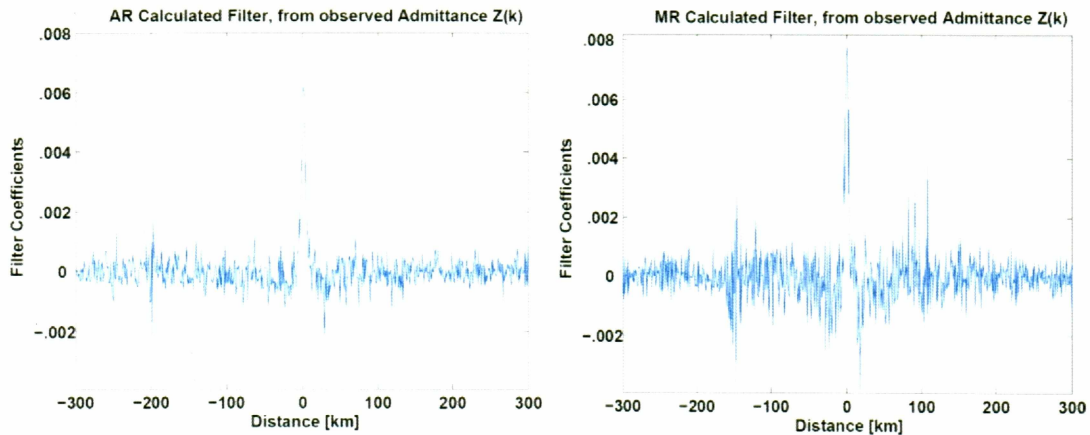


Figure 2.11: Lithospheric filters for AR (left) and MR (right), calculated by inverse FFT from gravitation admittance into spatial domain. The central 600 km about the ridge axis is plotted here. Reduced noise of the AR compared to the MR due to the number of profiles stacked can be seen between the two plots.

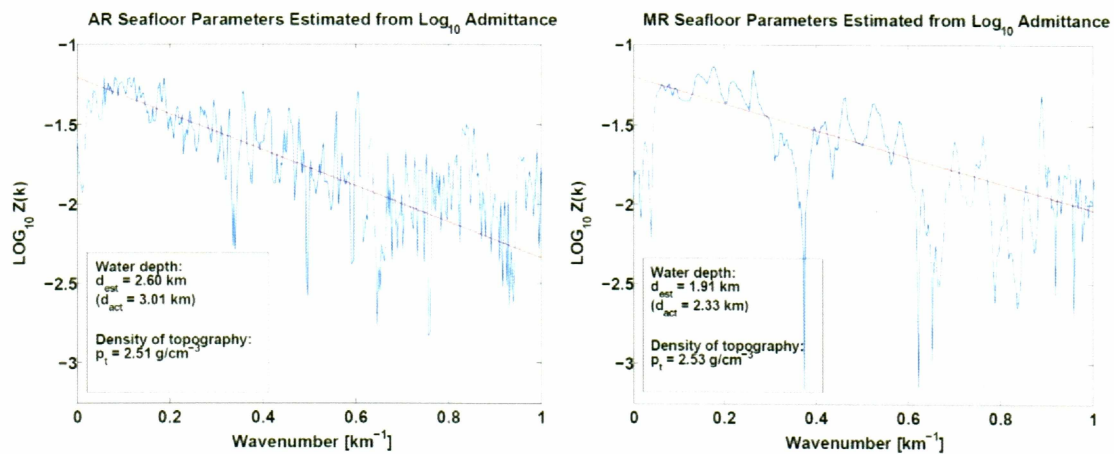


Figure 2.12:  $\text{Log}_{10}$  of the calculated admittance (blue) with linear fit (red) between  $0.008 < k < 0.6 \text{ km}^{-1}$  for the AR (a) and MR (b). Actual and estimated values are listed in each table. The average depth over the ridge sections differs, and estimates of water depth are underestimated relative to actual values. Both fits return similar densities of topography, consistent with the density of seafloor sediments.

#### 2.4.2 Isostatic Models for Alpha and Mendeleev Ridges

To quantify isostatic differences between the ridges we return to the isostatic models from Parker 1972 as outlined in section 2.3.2. Starting with the models of Airy isostasy, in figure 2.13 it is clearly seen that the MR and the AR do not fall within the same range of isostatic models. The best local isostatic model for the AR closely



resembles that of the entire ridge presented in the previous section, which makes sense because the AR makes up two-thirds of the profiles stacked to produce the AMR result. The best fitting model indicated by the black line is the local isostatic model with an average crustal thickness of 30 km and an average crustal density of  $2.8 \text{ g-cm}^{-3}$ , compared to the result from the AMR of thickness 25 km and density  $2.8 \text{ g-cm}^{-3}$ . The reduced  $\chi^2$  for this fit is higher than that for the AMR, likely due to fewer profiles going into the stacking process and thus having a higher noise content.

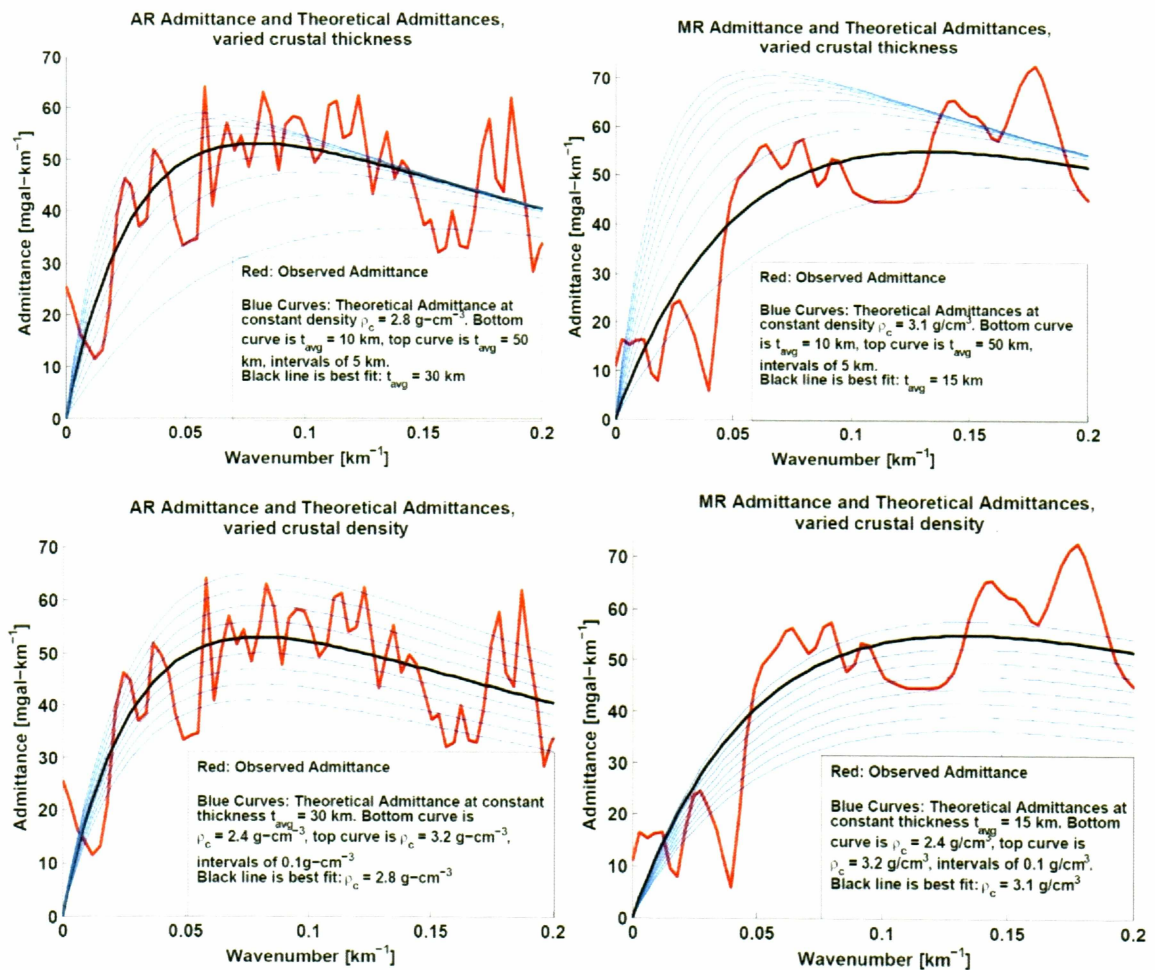


Figure 2.13: Observed admittance (red) with a set of theoretical Airy models (blue), for AR (left column) and MR (right column). Top figures are shown at constant density  $\rho_c = 2.8 \text{ g-cm}^{-3}$  for the AR,  $3.1 \text{ g-cm}^{-3}$  for the MR, with average crustal thickness varied from 10 to 50 km at intervals of 5 km. Bottom figures are at constant thickness  $t_{\text{avg}} = 30 \text{ km}$  for the AR and 15 km for the MR, with density varied between  $\rho_c = 2.4 - 3.2 \text{ g-cm}^{-3}$  at intervals of  $0.1 \text{ g-cm}^{-3}$ . All constant values held according to best fit models, shown as black curve.

The results for local isostasy for the MR however produce a best fitting model of average crustal thickness of 15 km and average crustal density of  $3.1 \text{ g-cm}^{-3}$ . This ridge thickness is not physically reasonable for a ridge in a Mesozoic basin whose thickness is already close to 15 km (Jackson and Johnson, 1986). If the best fit were true, then the ridge would be uncompensated. The results do not suggest this, as its admittance decreases at very low wavenumbers which indicates isostatic compensation. The resulting average density is also significantly high for either oceanic or continental crust, as this density is more characteristic of deep crust or high grade metamorphic rock. In addition, these results do not agree with previous studies over the AR (Forsyth et al., 1986a; Weber, 1990; Asudeh et al., 1988) and most definitely do not agree with more current studies of the MR (Lebedeva-Ivanova et al., 2006; Dove et al., 2006).

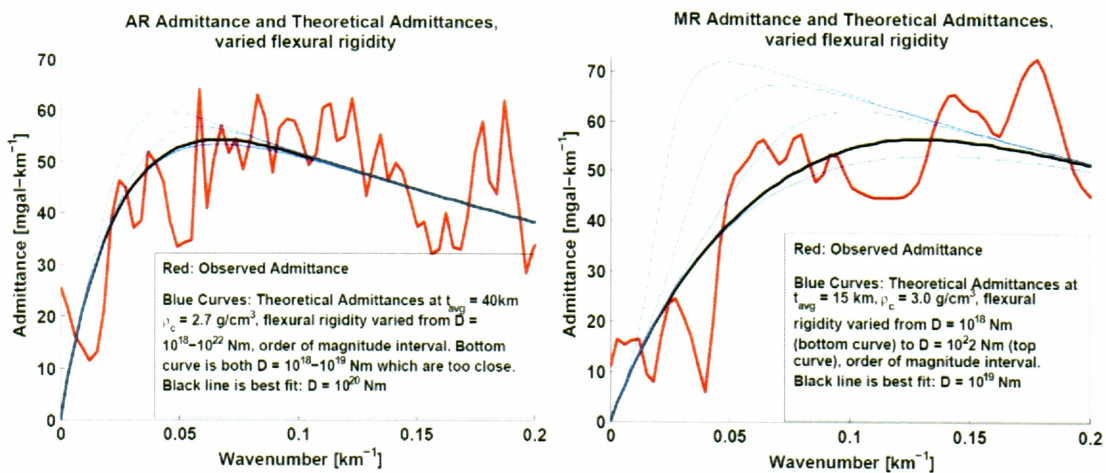


Figure 2.14: Observed admittance (red) with a set of theoretical flexure models (blue), for the AR (left) and the MR (right). For the AR, models shown left are at constant density  $\rho_c = 2.7 \text{ g-cm}^{-3}$ ,  $t_{\text{avg}} = 40 \text{ km}$  and varying flexural rigidity  $D = 10^{18} - 10^{22} \text{ Nm}$ . For the MR, models shown right at constant density  $\rho_c = 3.0 \text{ g-cm}^{-3}$ ,  $t_{\text{avg}} = 15 \text{ km}$  and varying flexural rigidity  $D = 10^{18} - 10^{22} \text{ Nm}$ . All constant values held according to best fit models, shown as black curve

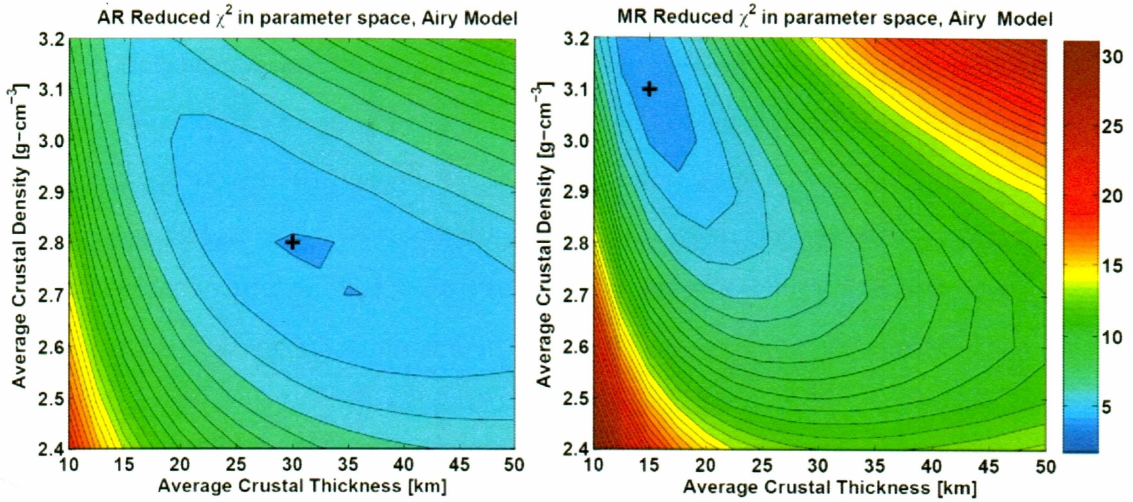


Figure 2.15: Reduced  $\chi^2$  in parameter space for the Airy isostatic model for the AR (left) and the MR (right). Average crustal thickness is plotted vs. average crustal density, the cross shows the location of the best fit model. For the AR this is at  $t_{\text{avg}} = 30$  km,  $\rho_c = 2.8$  g-cm $^{-3}$  which returns a reduced  $\chi^2 = 4.78$ , and for the MR,  $t_{\text{avg}} = 15$  km,  $\rho_c = 3.1$  g-cm $^{-3}$  with  $\chi^2 = 4.23$ .

The results for flexural isostasy are similar. Contours of  $\chi^2$  for the three best flexural rigidities for the AR are presented in figure 2.16. As with the Airy model, the results for the AR are not significantly different from the entire AMR. Most of the stacked profiles are from the AR. The best fitting model is the flexural model with average crustal thickness of 40 km and density of 2.7 g-cm $^{-3}$ . The flexural results from the AR, like for the entire AMR, fit slightly better than for local isostasy, and the flexural rigidity is extremely low, as  $T_{\text{eff}} = 2.24$  km, and thus approximates the Airy condition. The results for regional isostasy for the MR do not fit any better than local isostasy, and are shown in figure 2.17. Like the Airy case, the best fit region for the MR in parameter space does not converge within reasonable densities and thicknesses for lithosphere and even for mantle. The best fitting model has parameters  $t_{\text{avg}} = 15$  km,  $\rho_c = 3.0$  g-cm $^{-3}$  and  $D = 10^{19}$  Nm, corresponding to  $T_{\text{eff}} = 0.88$  km which approximates the Airy case. The observed admittances are shown with a range of parameters in figure 2.12 for Airy isostasy and 2.13 for flexural isostasy for both ridges. A summary of the goodness of each fit is presented in table 2.1. The reduced chi squared is much lower for the AMR

than for the separate AR and MR, suggesting that the analysis from the AR and MR were more sensitive to increased noise, possibly from an inadequate number of profiles used in stacking.

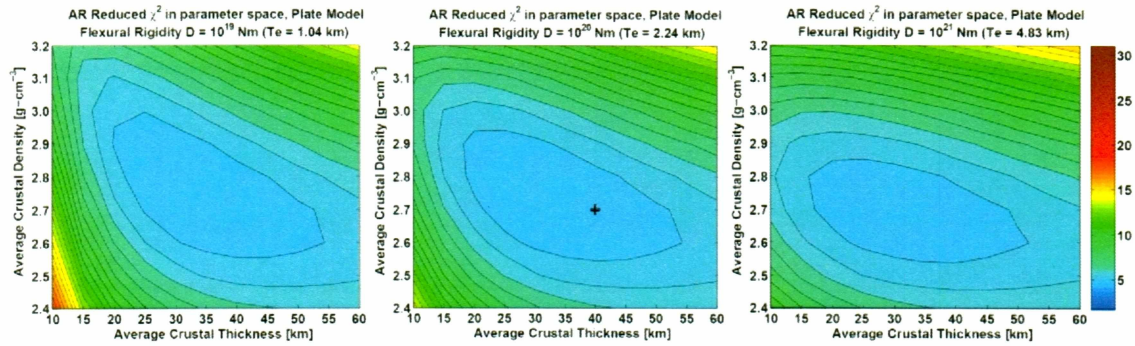


Figure 2.16: Reduced  $\chi^2$  in parameter space for the flexural isostatic model for the AR. Because three parameters are free in this model a range of plots is presented to show how the  $t_{\text{avg}}$  vs.  $\rho_c$  changes with flexural rigidity. The best fitting flexural rigidity is shown in the center plot with an order of magnitude change in flexural rigidity from left and right. The cross in the center plot shows the location of the best fit model with and reduced  $\chi^2 = 4.82$  at  $t_{\text{avg}} = 40\text{km}$ ,  $\rho_c = 2.7\text{ g-cm}^{-3}$  and  $D = 10^{20}\text{ Nm}$ , corresponding to an effective elastic thickness  $T_{\text{eff}} = 2.24\text{ km}$ , which is low for ordinary oceanic crust.

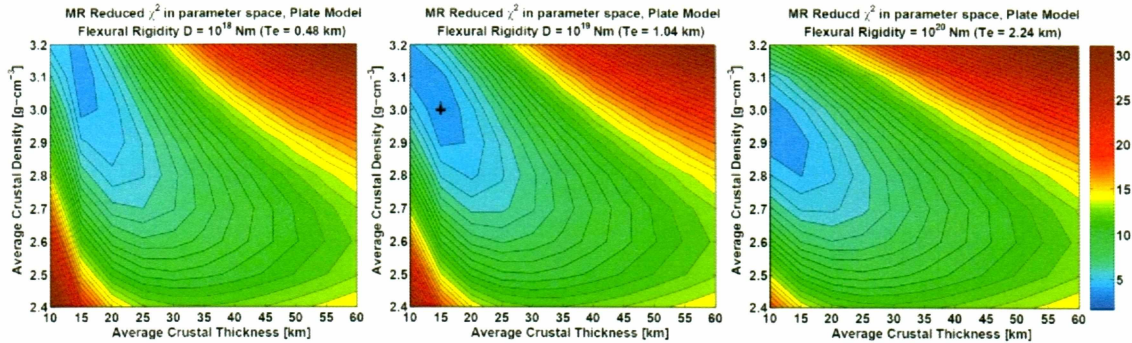


Figure 2.17: Reduced  $\chi^2$  in parameter space for the flexural isostatic model for the MR. Because three parameters are free in this model a range of plots is presented to show how the  $t_{\text{avg}}$  vs.  $\rho_c$  changes with flexural rigidity. The best fitting flexural rigidity is shown in the center with an order of magnitude change in flexural rigidity from left and right. The cross in the center plot shows the location of the best fit model with and reduced  $\chi^2 = 4.06$  at  $t_{\text{avg}} = 15\text{km}$ ,  $\rho_c = 3.0\text{ g-cm}^{-3}$  and  $D = 10^{19}\text{ Nm}$ , corresponding to an effective elastic thickness  $T_{\text{eff}} = 0.88\text{ km}$ , which is extremely low and essentially represents the Airy case, a crust with no strength.

Table 2.1: Summary of results of best isostatic models for each ridge analysis.

<b>Alpha-Mendelev Ridge</b>	<b>Avg thickness</b>	<b>Avg Density</b>	<b>Flexural Rigidity</b>	<b>Reduced <math>\chi^2</math></b>
Airy Model	25 km	2.8 g-cm <sup>-3</sup>	n/a	1.74
Plate Model	20 km	2.8 g-cm <sup>-3</sup>	10 <sup>20</sup> Nm	1.60
<b>Alpha Ridge</b>				
Airy Model	30 km	2.8 g-cm <sup>-3</sup>	n/a	4.78
Plate Model	40 km	2.7 g-cm <sup>-3</sup>	10 <sup>20</sup> Nm	4.82
<b>Mendelev Ridge</b>				
Airy Model	15 km	3.1 g-cm <sup>-3</sup>	n/a	4.23
Plate Model	15 km	3.0 g-cm <sup>-3</sup>	10 <sup>19</sup> Nm	4.06

## 2.5 Discussion of Results

From the analysis of separate ridge sections, the data suggests different isostatic mechanisms for each ridge as the isostatic signal from the MR is very distinct from that of the AR. However, the results of the spectral analysis of the MR data only have not suggested a reasonable isostatic model, and so the resulting isostatic differences between ridge sections are inconclusive. We suggest this is not due to the MR having a strange mechanism of isostasy, but rather that the available data over this ridge was not sufficient to carry out such a calculation for several reasons. First, three profiles may not be enough data to reduce the noise in this case. Second, the crowded environment in which the MR lives may significantly complicate the gravity signal. This would violate the assumption that the source of the gravity signal is attributed only to the ridge and basin. The MR is attached to a heavily sedimented area sloping off the continental shelf, possibly too close to the attachment of both the Chukchi Plateau, and the Lomonosov Ridge, while large portions of the AR are adjacent to deep basins where the gravity effect of isostasy should be visible. The adjacent features are close enough that they may be influencing the gravity measurements taken there. Third, the data from each ridge differ in several ways, including that the profiles over the MR are on average bathymetrically higher, in addition

to the fact that the endpoints of the profiles do not cross into the true basin the way they do over the AR.

In light of the shortcomings of the MR results, another test is needed to determine any differences in the structure of these two ridges. Because the admittance from the MR is physically unreasonable, this may have affected the stacking of profiles for the whole AMR. While most of the profiles used in the stacking for the AMR are from the AR, it makes sense that the AMR admittance would resemble the AR admittance. This is apparent in the results, with the exception of a decrease in the average thickness for the AMR. It can be seen that the much lower average thickness returned for just the MR in the stacking process may be influencing the AMR results. This should be taken into consideration, since the MR profiles should not be used if they do not produce physically reasonable results in spectral analysis. As a result, the results for the AMR may not be valid either, and it cannot be ruled out that the MR has the same overall structure as the AR. As a final test of these results, chapter three will calculate the gravity signal of a crustal section using the isostatic models for the AMR and AR. This gives a second opportunity to test differences in ridge sections.

## **2.6 Data Grids**

In light of the conclusions from the shiptracks, the analysis was also done for more commonly available gridded datasets over the Arctic. The International Bathymetric Chart of the Arctic Ocean (IBCAO), and the Arctic Gravity Project (AGP), are free for download from the websites mentioned in section 1.3. The IBCAO grid includes surface and submarine echo sounding data. The submarine measurements are a compilation from U.S. and British nuclear submarine expeditions between 1958-1988, and from nuclear submarines during the Science Ice Exercise (SCICEX) program between 1993-1999 (Edwards and Coakley, 2003). The data from surface vessels come from the US National Geophysical Data Center, US Naval Research Laboratory, the Canadian Hydrographic Service and the Royal Danish Administration of Navigation and

Hydrography (Jakobsson et al., 2000). A smaller portion of the shiptracks come from the icebreakers *Oden* in 1991 and 1996, and *Polarstern* in 1995.

The AGP data are a combination of shipborne (Edwards and Coakley, 2003) and airborne gravity measurements (Childers et al., 2001) as well as satellite derived gravity (Laxon and McAdoo, 1994) contributed from a host of participating circumpolar countries (Kenyon and Forsberg, 2001). One dimensional profiles were sampled from the gridded gravity anomaly and bathymetry datasets used in this study. The sampled data are at evenly spaced intervals of one kilometer from the grids perpendicular to the ridge axis, using the Generic Mapping Tool (GMT) bilinear interpolation. The twenty-seven one-dimensional profiles of gravity and bathymetry sampled from the grid for this study are shown on the map in Figure 2.18. Profile locations were defined using their endpoints and constructed by sampling and interpolating points from the grids.

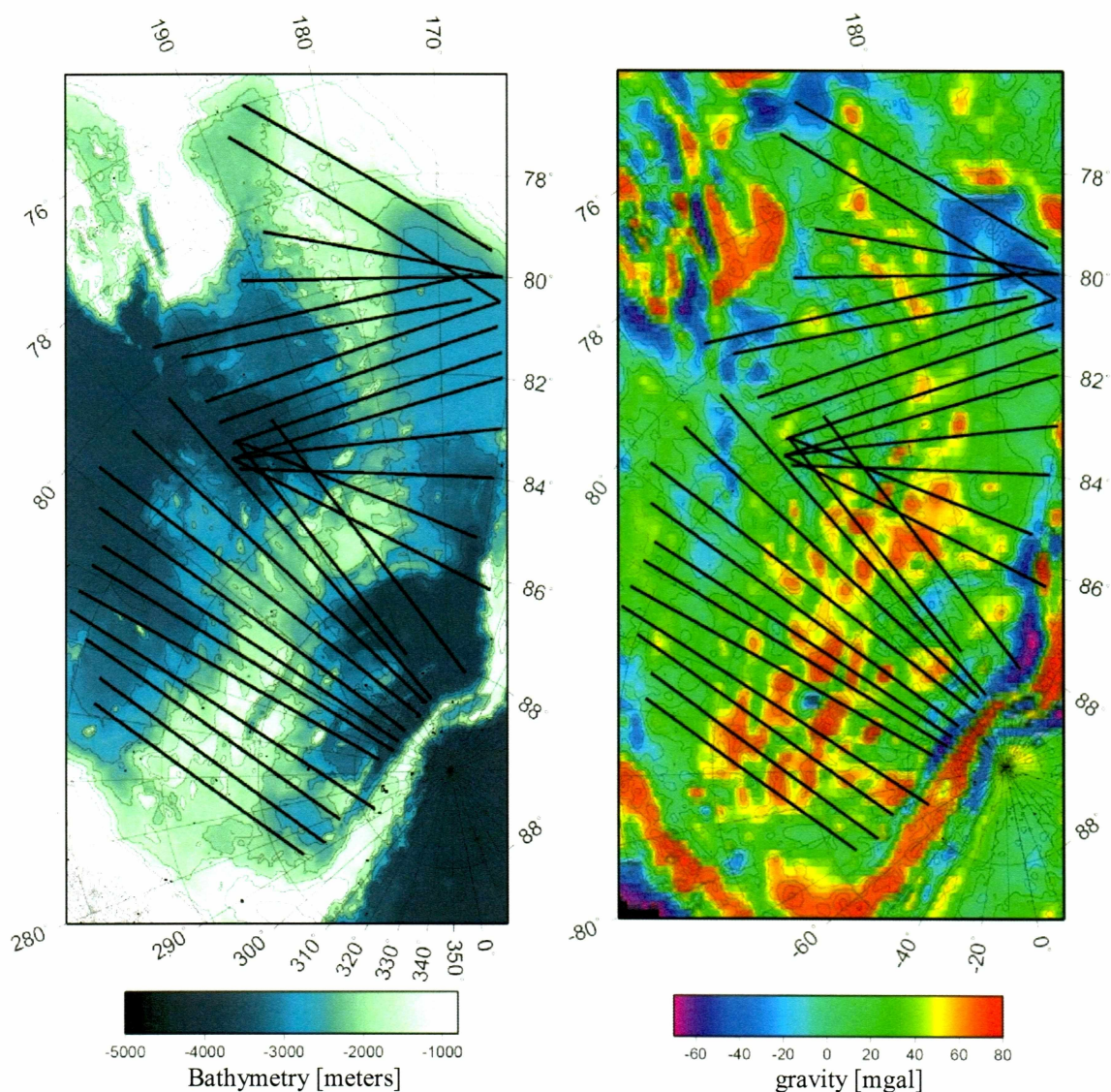


Figure 2.18: Locations of 27 profiles sampled from the IBCAO and AGP data grids.

The results of the spectral analysis using the gravity and bathymetry grids are summarized here. The gravitational admittance was calculated for the entire AMR. The admittance does not fit any of the theoretical models presented in Watts (2001), or any of the observed data presented over other oceanic features in the literature. In addition the estimated seafloor parameters from the calculated admittance are physically unreasonable for oceanic crust, as shown in figure 2.19. For example, the estimated water depth over the profiles is 3.99 km whereas the actual average water depth is 2.60 km. Furthermore



the estimated density of the topography of the ridge is  $1.6 \text{ g-cm}^{-3}$  which is unreasonable for sediments, not to mention oceanic or continental crust. Linear fits to other wavenumber ranges do not improve the average seafloor depth and density estimates. For example, fit to the wavenumber range of  $0.12 < k < 0.24$  where the plot appears linear returns an average seafloor depth of 12.43 km. Constraining the average seafloor depth returns approximately the same density of topography. Such a low density also disagrees with the densities of geologic samples obtained from dredging of the AMR during the CESAR mission, (Mudie et al., 1986) as well as results from previous gravity modeling projects (Sweeney and Weber, 1986) and seismic investigations (Asudeh et al., 1988; Jokat, 2003).

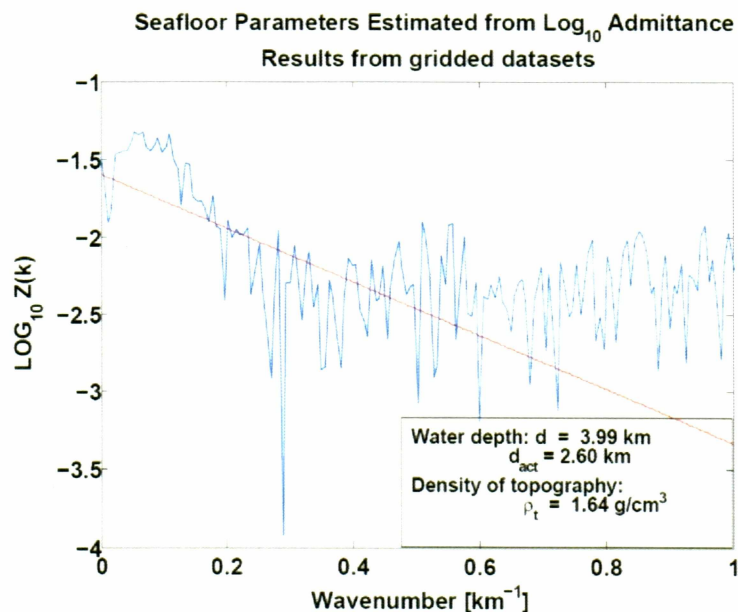


Figure 2.19:  $\text{Log}_{10}$  of the calculated admittance (blue) with linear fit (red) between  $0.008 < k < 0.6 \text{ km}^{-1}$  as described in Watts 2001. Linear trend in  $\text{Log}_{10} Z$  does not correspond to the proper wavenumber range listed above. Water depth and crustal density estimated from the fit do not compare well with actual and realistic values.

In addition, the best fitting isostatic models, shown in figure 2.20, disagree with the shiptrack results. The admittance only fits theoretical models out to  $k = 0.1 \text{ km}^{-1}$ , the beginning of the region at which topography and gravity should be correlated. In this region the cross spectrum is flat, indicating the signals in the original datasets are only

noise. As this is also the wavenumber region where uncompensated topography is significant in the isostatic signal, as should be seen in figure 2.19, it can be concluded that the shorter wavelength features in the grids are not correlated as they should be.

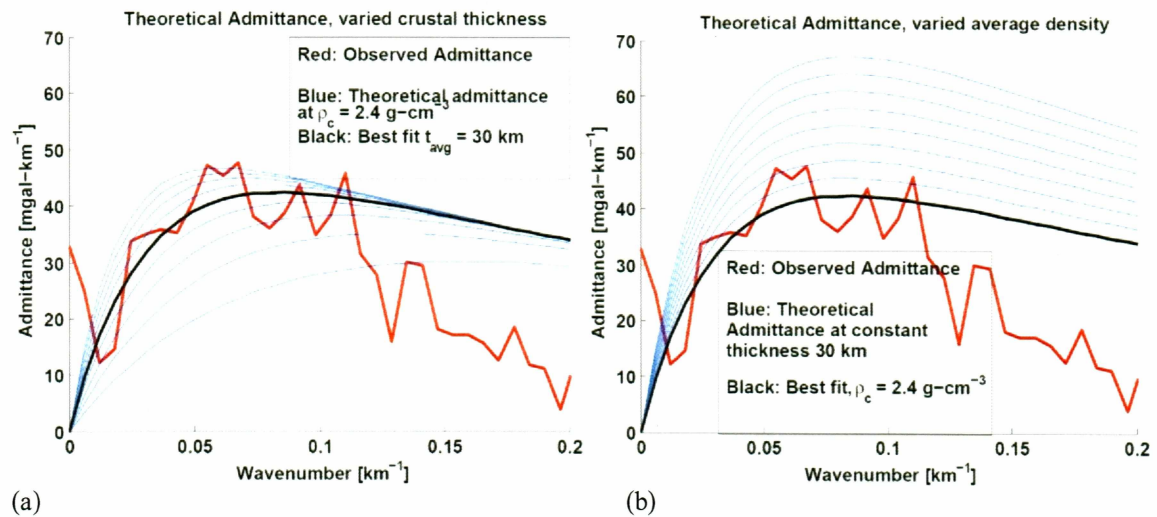


Figure 2.20: (a) Observed grid admittance (red) with a set of theoretical Airy models (blue) at constant density  $\rho_c = 2.4 \text{ g-cm}^{-3}$ . Average crustal thickness is varied from 10 to 50 km at intervals of 5 km. (b) Observed admittance with Airy models at constant thickness of 30 km and density varied from 2.4 to 3.2  $\text{g-cm}^{-3}$  with intervals of 0.1  $\text{g-cm}^{-3}$ . The observed admittance deviates from the isostatic models at approximately  $k = 0.12 \text{ km}^{-1}$ , indicating the limiting resolution of the grids.

Further examination of the relationship between the two gridded datasets may explain why they produce such noisy results, and are unsuitable for spectral analysis. The source datasets for the grids have different resolutions, which vary, according to the distribution of data sources over the Arctic. This is partially due to the large differences in resolution and distribution of the underlying measurements, for example, the gravity measurements below 81°N are from satellite altimetry (Laxon and McAdo, 1994), that is relatively low resolution (Childers et al., 2001), whereas much of the bathymetry comes from submarine shiptracks and are thus higher resolution but less densely sampled. In addition, sparse and unevenly distributed bathymetry datapoints were used to construct the IBCAO grid. As a result, profiles interpolated from the continuous grid may not have many nearby source datapoints to support them. In fact, the grid sampled gravity highs and lows do not mimic the topographic highs and lows from the grid sampled

bathymetry, as would be expected for normal oceanic bathymetry. Instead the frequency of highs and lows appear to be phase shifted, shown in figure 2.21, something that is not observed in other datasets over the AMR (figure 2.2). This is likely the reason that the admittance signal becomes noise in the wavenumber range where topography and gravity should be correlated, and why the spectral analysis yielded inconclusive results.

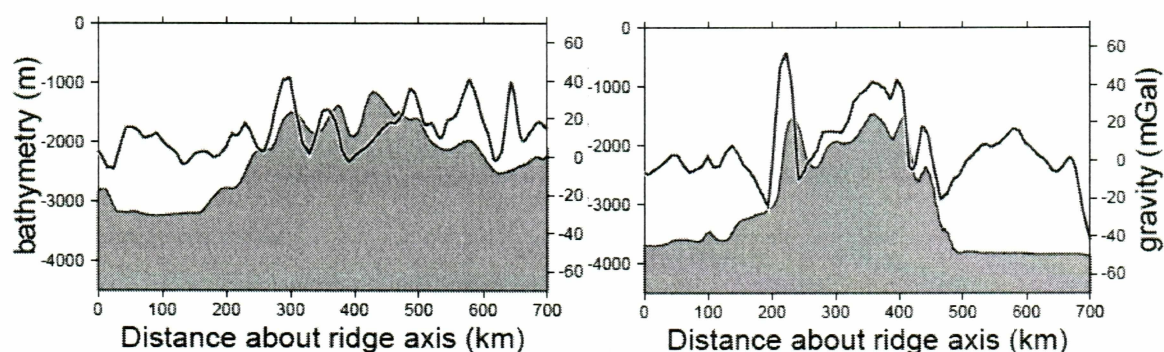


Figure 2.21: Two examples of the grid sampled gravity (line) and bathymetry (grey fill) profiles. The phase shift seen between gravity and topographic highs are present in the majority of the grid sampled profiles. This reflects the errors in bathymetry from submarine inertial navigation and older icebreaker data (pre-GPS), vs. the GPS navigated airborne gravity and satellite gravity data.

### **3. GRAVITY MODELING**

#### **3.1 Introduction**

Although the spectral analysis from the gridded datasets yielded no results, the results from the shiptracks discussed in section 2.5 still need to be tested. Using the observed gravity it is possible to estimate the mass distribution in the crust that may produce the gravity signal, but there is no unique solution to such a problem (Blakely, 1996). With profiles of observed bathymetry, it is simpler to calculate a theoretical gravity profile by forward modeling a density configuration in the crust, using the constraints from spectral analysis, to compare with the gravity that was observed. An isostatic model using bathymetry which calculates a gravity signal that closely resembles that observed over the same shiptrack will validate the results from the previous chapter.

#### **3.2 Methods**

##### **3.2.1 2-D Shiptrack Models**

A two dimensional crustal cross section is constructed based on the shiptrack bathymetry and isostatic model derived from spectral analysis in the previous section. The cross section runs perpendicular to the strike of the ridge and down with depth in the crust. A theoretical gravity profile is calculated by forward modeling of the two dimensional cross section and can be used to compare to the observed shiptrack gravity data. The gravity calculation is run using the software GM-SYS from Northwest Geophysical Associates, which follows the line integral techniques and methods of Talwani et al. (1959) and the algorithm for calculating potential anomalies of polygons from Won and Bevis (1987). In this way the isostatic model found in the last section can be tested to see how well it reproduces the observed gravity for each shiptrack. The projected shiptracks used are the same as for the spectral analysis.

The crustal cross section is constructed with the observed bathymetry as the water-topography density interface, and the crust-mantle interface as defined in the

spectral analysis results for the AR and the entire AMR. These results suggest the AMR is compensated by Airy isostasy with a crustal density of  $2.8 \text{ g-cm}^{-3}$  and an average crustal thickness of 30 and 25 km respectively. The crust-mantle boundary is calculated using the bathymetry by assuming airy isostasy and a constant average crustal thickness over all profiles. In addition, to make the marine environment more realistic and improve the fit, a uniform layer of sediments 1 km thick and of density  $2.5 \text{ g-cm}^{-3}$  as suggested from the spectral analysis was added to each profile and local thicknesses were adjusted. It is noted that introducing sediments and adjusting the sediment thickness do not significantly change the overall state of isostasy of the ridge and are mostly added to local troughs where sediment is more likely to slump and collect. Such small and localized changes in mass in the crustal column are not compensated and so should not affect the overall isostasy. In some cases slightly thicker sediments were introduced in the basin environment to improve the gravity fit.

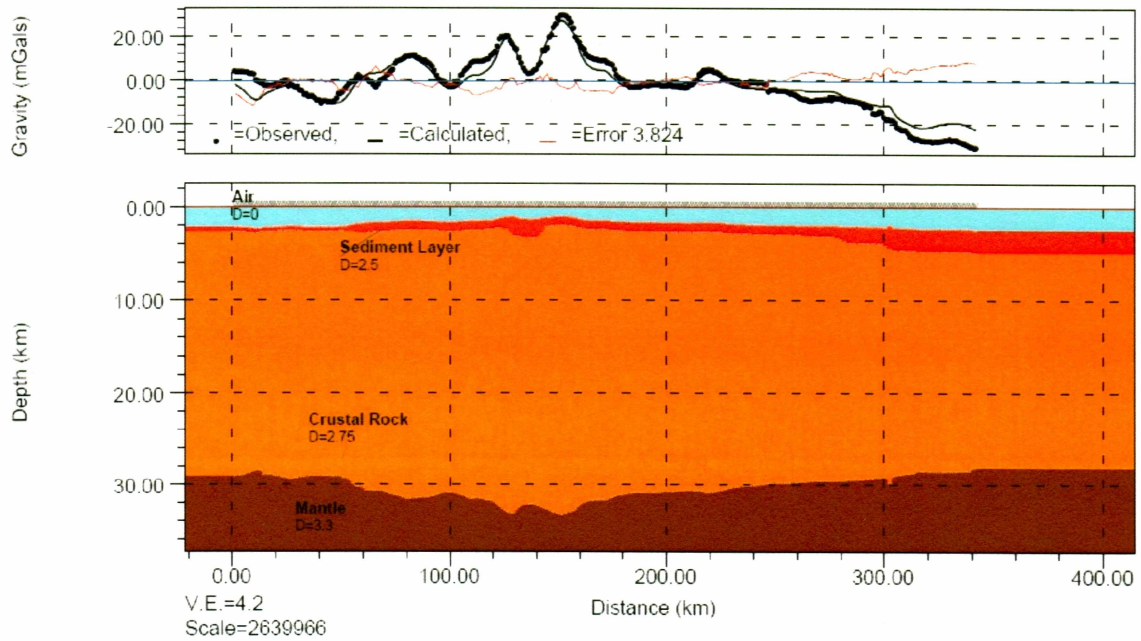
### **3.3 Results**

#### **3.3.1 2-D Crustal Models**

Overall, the anomalies over the ridge crest can be fairly well explained by the crustal models. Anomalies over the adjacent basins in general do not fit as well as those over the ridge. In an attempt to fine tune the results from the spectral analysis, the thickness and average density in the models were changed slightly to find the set that predicts the gravity with the lowest overall residual. The isostatic results from the MR spectral analysis do not correspond well to the observed gravity, further suggesting these results are nonsensical. The results from just the AR of thickness 30 km produced better fits than the estimate from the entire AMR of 25 km, which makes sense if the admittance contribution from the MR profiles were not physically reasonable. Therefore, the results from the MR were not included in the modeling results and an average thickness of 30 km is used. These are plotted for all nine shiptracks in figure 3.1. It was found that over the whole AMR, with average thickness of 30 km and density of  $2.75 \text{ g-cm}^{-3}$  produced the set of gravity models with the lowest residual.

Some deviations between the observed and predicted gravity remain. This is particularly evident in profile B. For all permutations of the crustal structure, the misfit over profile B was higher than for the rest of the profiles. It is the only profile whose goodness of fit improved when drastically decreasing the average density from that estimated by spectral analysis. However, the goodness of fit could also be improved by introducing a fragment of lower density beneath the misfit area on the right half of the ridge. This could be evidence of heterogeneity within the ridge, possibly indicating the ridge contains large fragments of lower density. All other profiles follow the same trend in crustal structure, including A and C, the other two profiles over the MR. These observations suggest that profile B is an anomaly among the AMR profiles, and the other eight profiles may carry more weight in their results. For the other profiles, the majority of the misfit is from the part of the profile that crosses the basin. In most cases the fit over the ridge is very good. The locations of the largest misfits are not consistent for all profiles, and so are considered to be local variations due to the two-dimensional representation, but not a fault of the overall isostatic model in representing the ridge structure. The residuals for the models using different densities are summarized in tables 3.1 and 3.2.

### Profile A (MR)



### Profile B (MR)

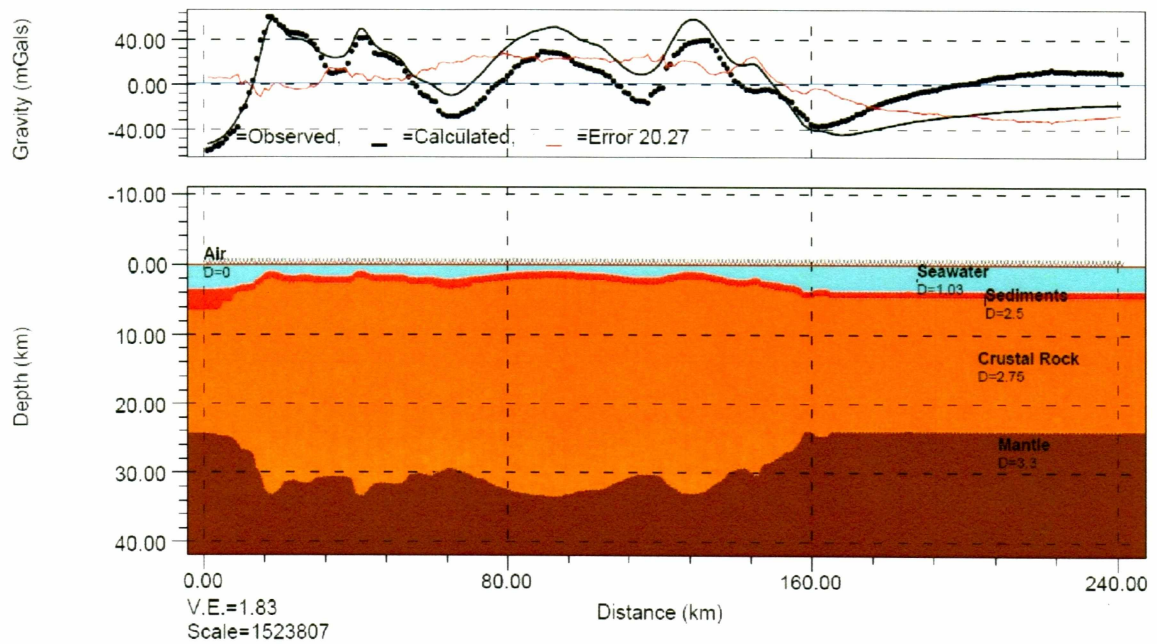


Figure 3.1 (A-I): Crustal models for the nine shiptracks. Densities used are  $1.03 \text{ g-cm}^{-3}$  for seawater (blue),  $2.5 \text{ g-cm}^{-3}$  for sediments (red),  $2.75 \text{ g-cm}^{-3}$  for crustal rock (orange), and  $3.3 \text{ g-cm}^{-3}$  for mantle (maroon).

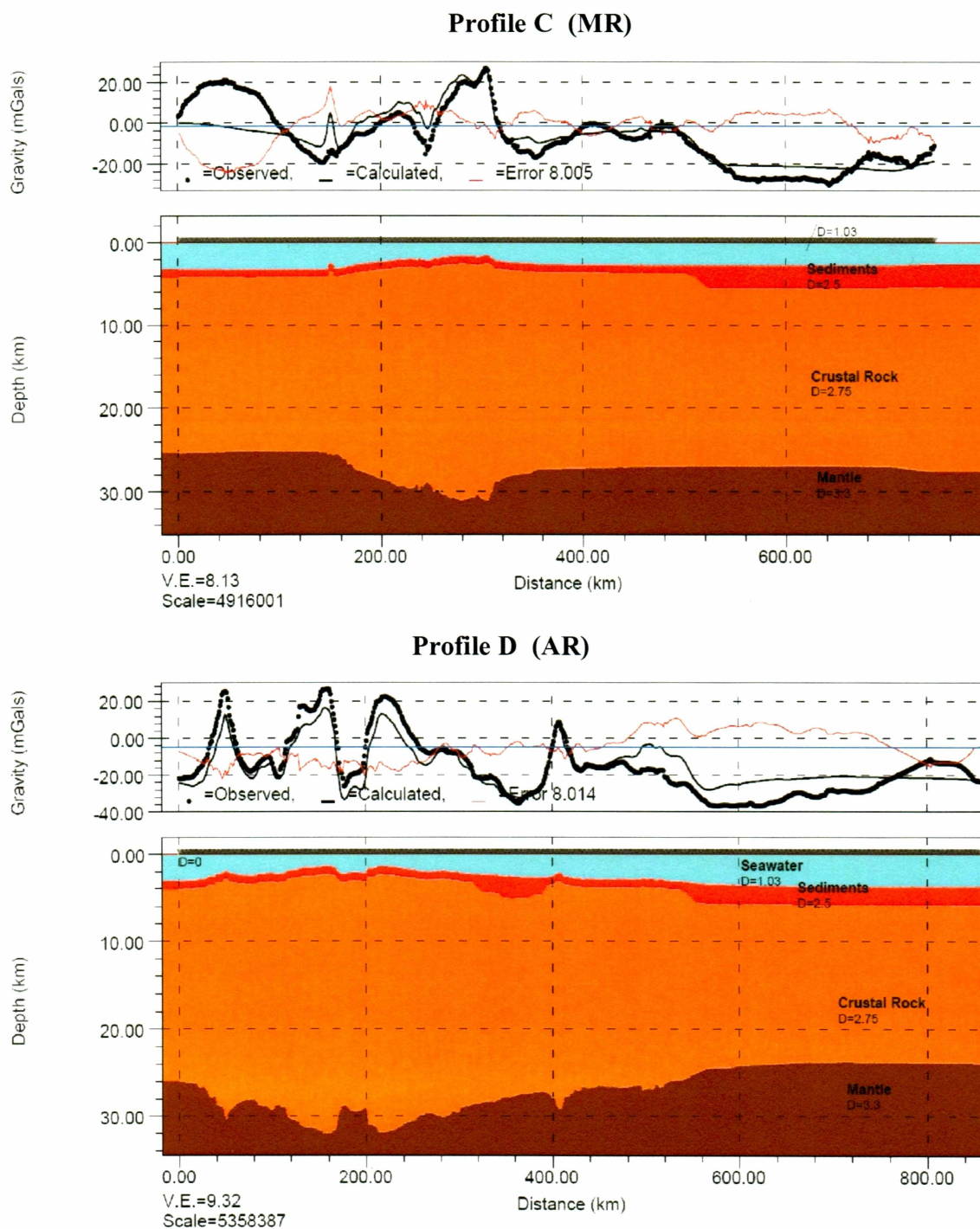


Figure 3.1 (A-I) Continued: Crustal models for the nine shiptracks. Densities used are  $1.03 \text{ g-cm}^{-3}$  for seawater (blue),  $2.5 \text{ g-cm}^{-3}$  for sediments (red),  $2.75 \text{ g-cm}^{-3}$  for crustal rock (orange), and  $3.3 \text{ g-cm}^{-3}$  for mantle (maroon).



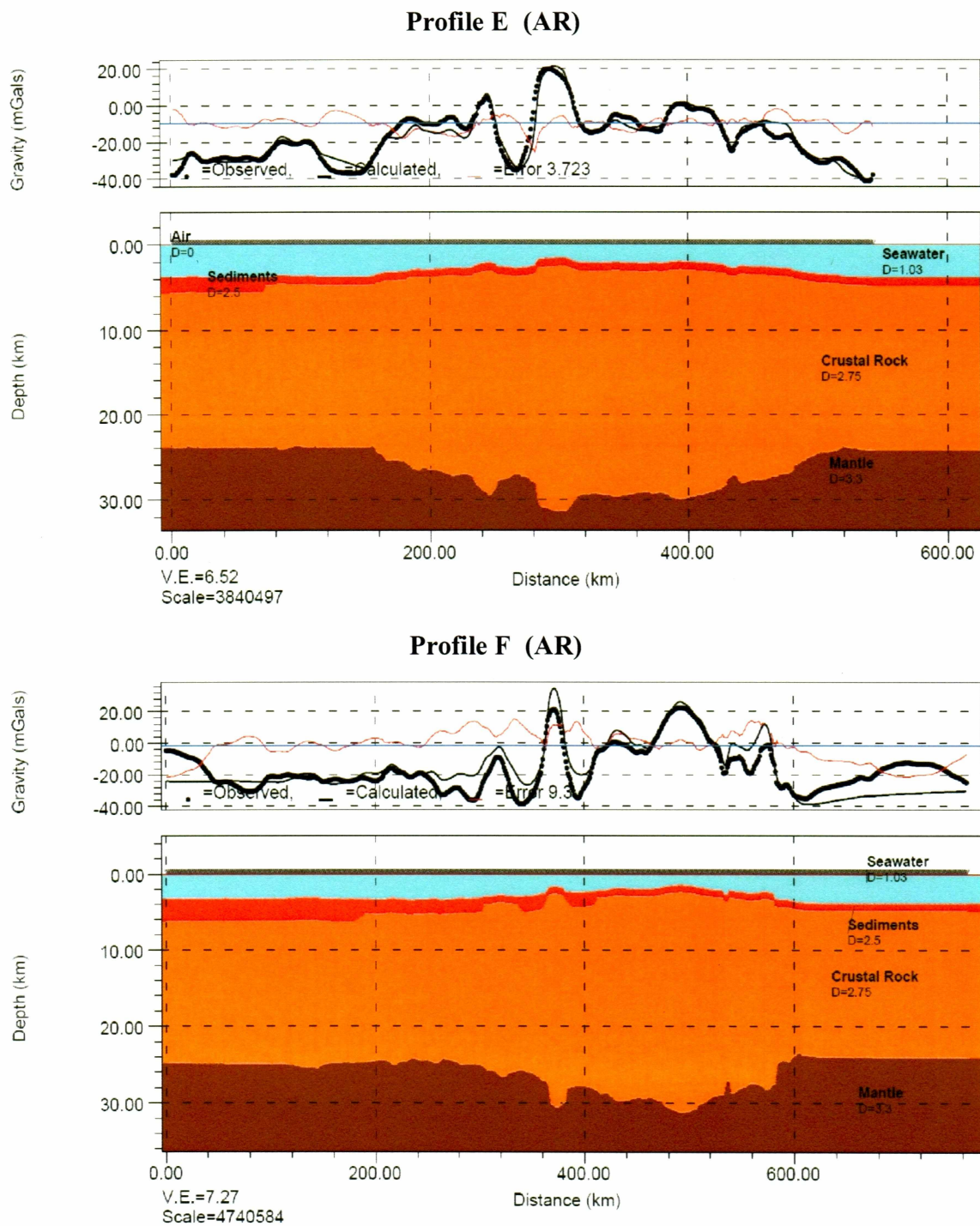


Figure 3.1 (A-I) Continued: Crustal models for the nine shiptracks. Densities used are  $1.03 \text{ g}\cdot\text{cm}^{-3}$  for seawater (blue),  $2.5 \text{ g}\cdot\text{cm}^{-3}$  for sediments (red),  $2.75 \text{ g}\cdot\text{cm}^{-3}$  for crustal rock (orange), and  $3.3 \text{ g}\cdot\text{cm}^{-3}$  for mantle (maroon).

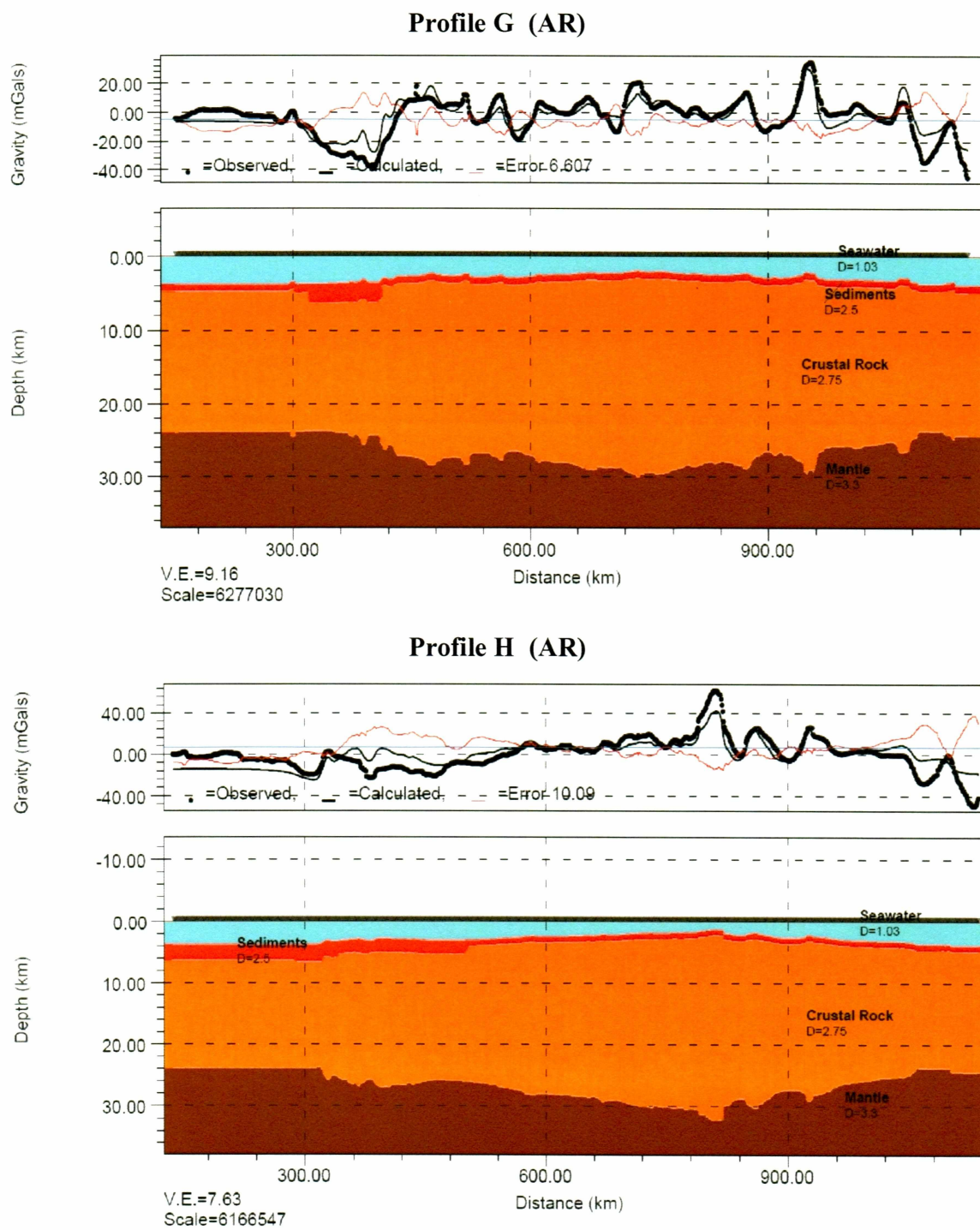


Figure 3.1 (A-I) Continued: Crustal models for the nine shiptracks. Densities used are  $1.03 \text{ g-cm}^{-3}$  for seawater (blue),  $2.5 \text{ g-cm}^{-3}$  for sediments (red),  $2.75 \text{ g-cm}^{-3}$  for crustal rock (orange), and  $3.3 \text{ g-cm}^{-3}$  for mantle (maroon).

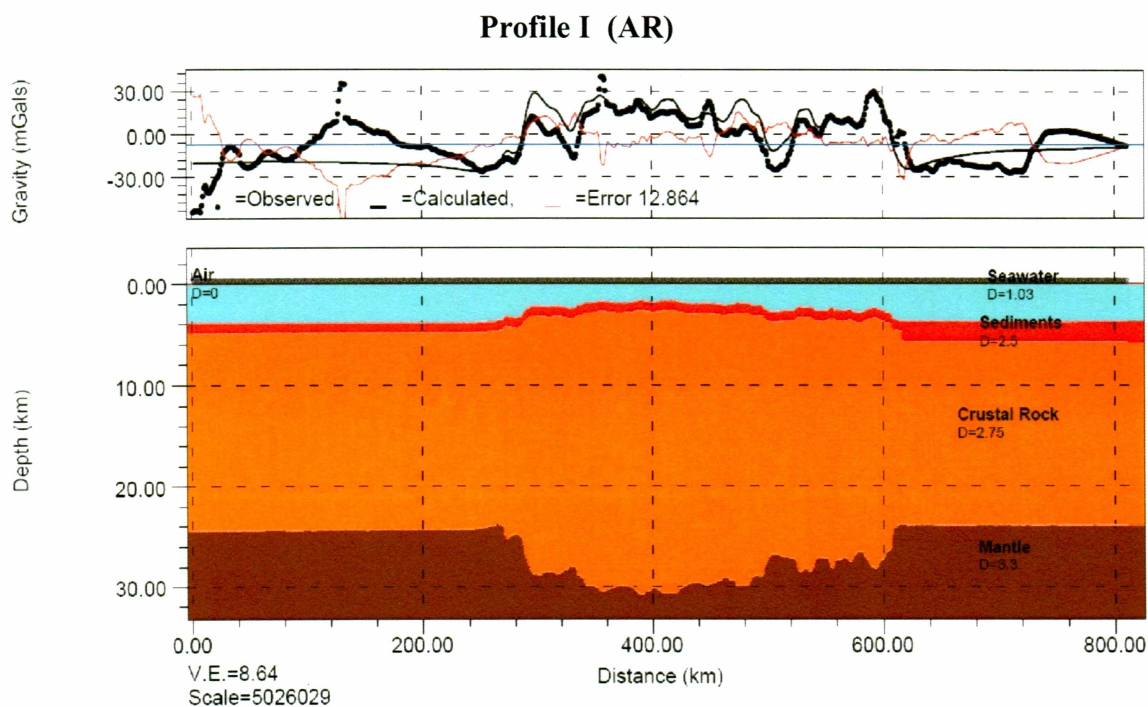


Figure 3.1 (A-I) Continued: Crustal models for the nine shiptracks. Densities used are  $1.03 \text{ g}\cdot\text{cm}^{-3}$  for seawater (blue),  $2.5 \text{ g}\cdot\text{cm}^{-3}$  for sediments (red),  $2.75 \text{ g}\cdot\text{cm}^{-3}$  for crustal rock (orange), and  $3.3 \text{ g}\cdot\text{cm}^{-3}$  for mantle (maroon).

Table 3.1: Summary of model misfits ( $\chi^2$ ) for crustal models of average thickness 30 km, including layer of tweaked sediment cover. Lowest average misfit of 9.185 occurs for density of  $2.75 \text{ g}\cdot\text{cm}^{-3}$ .

Density [ $\text{g}\cdot\text{cm}^{-3}$ ]		2.65	2.7	2.75	2.8	
Profile	A	8.878	6.173	3.824	2.893	
	MR	B	10.123	14.833	20.27	25.98
		C	8.221	7.33	8.005	9.931
		D	20.103	13.562	8.014	6.702
	AR	E	11.935	6.988	3.723	6.125
		F	10.329	8.214	9.268	12.718
		G	12.896	9.008	6.607	7.336
		H	16.964	12.442	10.09	11.348
		I	13.514	11.803	12.864	16.159
Average		12.551	10.039	9.185	11.021	

Table 3.2: Summary of model misfits ( $\chi^2$ ) with average thickness 30 km not including sediment cover. Lowest average misfit of 11.675 also occurs for density 2.75 g-cm<sup>-3</sup>

Density [g-cm <sup>-3</sup> ]		2.65	2.7	2.75	2.8
<b>Profile</b>					
	<b>A</b>	11.648	10.086	8.883	8.201
<b>MR</b>	<b>B</b>	10.695	15.453	20.927	26.68
	<b>C</b>	11.903	11.801	12.422	13.666
	<b>D</b>	27.774	19.587	11.607	9.01
	<b>E</b>	12.914	8.293	4.81	5.467
<b>AR</b>	<b>F</b>	13.803	12.212	12.259	13.928
	<b>G</b>	14.579	11.338	9.193	9.004
	<b>H</b>	19.42	15.013	11.373	9.435
	<b>I</b>	14.986	13.233	13.604	15.951
<b>Average</b>		15.302	13.001	11.675	12.371

As both the models with and without sediment cover suggest average density of 2.75 g-cm<sup>-3</sup>, it is reasonable to accept this as the average density for the AMR. As mentioned earlier, the average thickness of 30 km, as estimated from spectral analysis for the AR, appears to explain all profiles better than the thickness estimated from the AMR. The crustal modeling thus provides evidence that the whole AMR is compensated according to the local isostatic model found for the AR from spectral analysis. The overall goodness of fit over the whole ridge using one isostatic model for both ridge sections suggests the two ridges have the same crustal structure and may be one oceanic feature with the same origin.

### 3.3.2 Grid Crustal Models

Finally, the isostatic model tests were extended to include other datasets previously mentioned in section 2.6, the IBCAO bathymetry grid and AGP gravity grid. As GM-SYS can only handle inputs of one dimensional profiles, the forward modeling of gravity was carried out using the functions of GMT which can handle grids of data. The

constructed 3D crustal model is mathematically identical to the 2D shiptrack crustal models. The gravity calculation was done by making use of the GMT function *grdfft*, which can calculate the gravity signal due to a density interface at depth by using the first order expansion of Fourier methods from Parker (1972) of calculating gravity due to topography. *Grdfft* then upward continues the signal to sea level to match the observed measurements.

This calculation was applied to the IBCAO arctic bathymetry grid, to predict the gravity over a two dimensional area. The AGP gravity and predicted gravity for the AR and MR are shown in figures 3.2 and 3.3 respectively. In the plots the predicted gravity roughly follows the bathymetric highs and lows on the IBCAO grid as would be expected, however they do not correspond well to the highs and lows from the AGP. Their locations are different and the IBCAO overall underestimates the gravity highs in the AGP due to topographic highs by as much as 30 mgal. The biggest contribution to short wavelength marine gravity is the topographic surface, resulting from the closest large density contrast. This relationship is clearly apparent from the gravity models using the shiptracks shown in section 3.3.1, and it should be no different for the gridded data. However, as it was observed in section 2.2.1 when the admittance calculation was run on the profiles sampled from the grids, the inconsistency between the AGP and IBCAO was clear and inhibited both the isostatic calculation and gravity modeling.

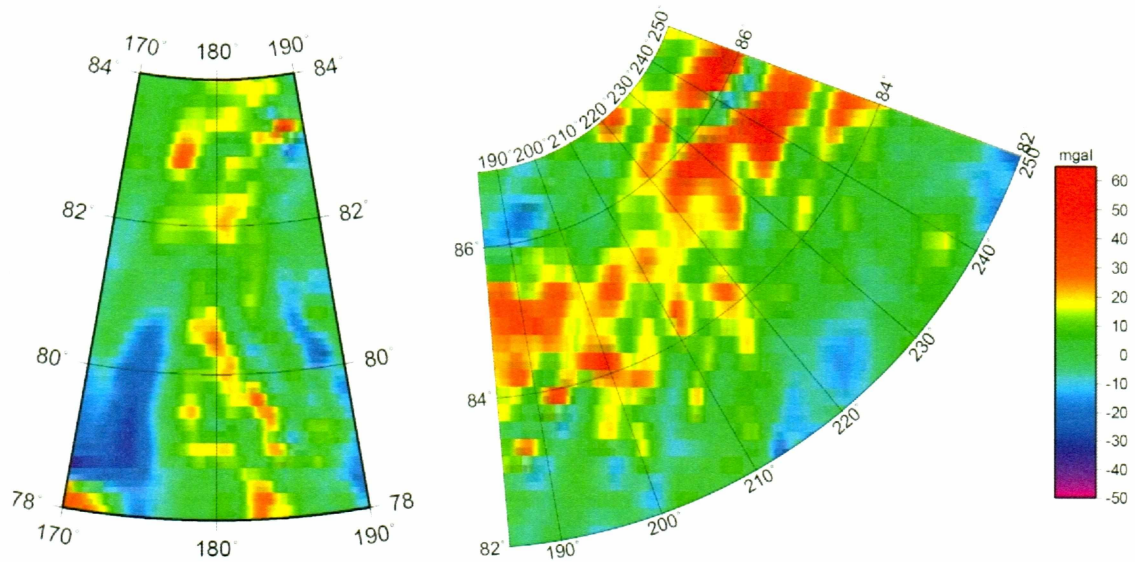


Figure 3.2: AGP gravity for the MR (left) and AR (right).

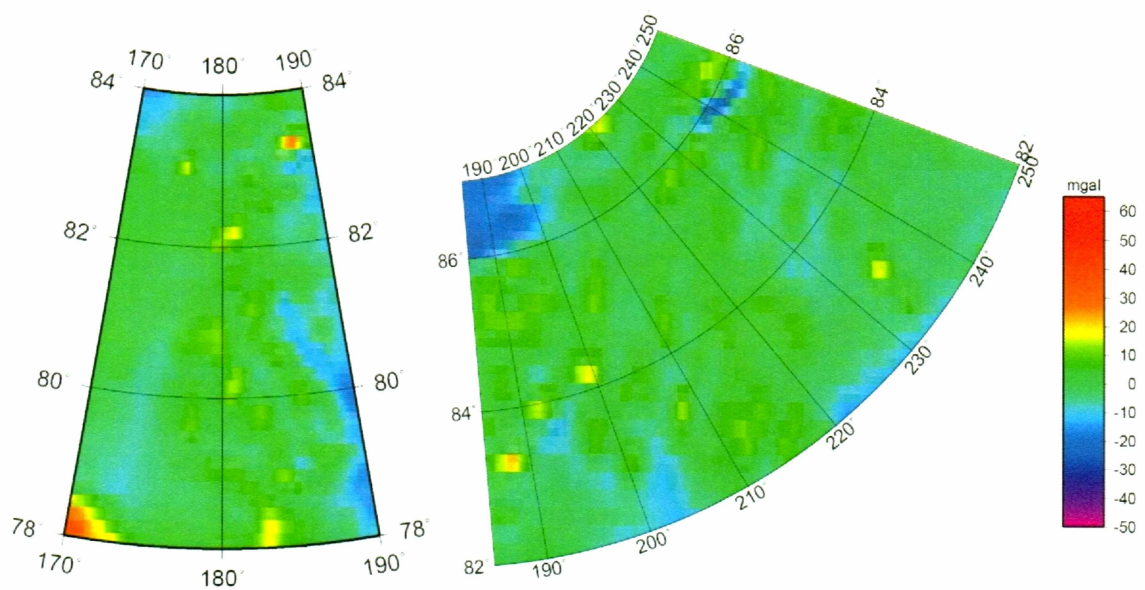


Figure 3.3: Predicted gravity for the MR (left) and the AR (right). Color scale plotted is the same for both AGP and predicted gravity maps.

I suggest the source of this problem lies in the density and uniformity of source data for the two grids. The IBCAO grid has a higher resolution than the AGP grid. But

while overall the IBCAO has regions of very densely sampled source data, in the vicinity of the AMR, the source data are very sparse and not uniformly sampled. In fact it is the least densely sampled region of the Arctic Ocean. In addition, because the IBCAO grid has a higher resolution than its source data around the AMR, the bathymetry data over the AMR is under-sampled and most points are interpolated. The IBCAO data sources are very different from the data sources in the AGP, which is primarily airborne and satellite gravity data and is thus more isotropic and in fact more densely sampled than the IBCAO around the AMR. This, combined with the inability of the bathymetry to reproduce the short wavelength features seen in the gravity signal, suggests that the IBCAO is not very representative of the short wavelength bathymetry around the AMR.

#### 4. DISCUSSION

The isostatic results from the spectral analysis over the AMR suggest it is compensated locally with an average crustal thickness of 25 km. When a dataset consisting of just the AR is used, an average crustal thickness of 30 km is determined, while the isostatic results from only the MR are inconclusive. We suggest the spectral analysis over the MR failed because only three profiles were available, and the basin environment of the MR is complicated by the presence of other oceanic features. In contrast to the more open AR, the MR is located in close proximity to the Chukchi Borderland and the Lomonosov Ridge. The three profiles from the MR lie very close to the continental shelf adjoining all three of these features and none of the profiles extend into the true basin where the gravity effects of isostasy should be apparent. Thicker sediments are present on the flanks and surrounding basins of the MR, in contrast to the AR. Complicated geology may conflict with assumptions necessary for the technique.

However, the crustal modeling of the shiptracks, which used the isostatic model for just the AR, are in fairly good agreement with the observed gravity over both the MR and the AR, suggesting that the MR is likely to be locally compensated with a very similar structure to the AR of average density  $2.75 \text{ g-cm}^{-3}$  and average thickness of 30 km. This roughly agrees with previous studies which pin the maximum depth beneath the ridge crest to be 32 km for the MR (Lebedeva-Ivanova et al., 2006) and 38 km for the AR (Forsyth et al., 1986a). Since the AMR can be described using one isostatic model and crustal structure, it is possible these features are in fact one continuous ridge with the same tectonic origin.

With a broader tectonic context, this crustal structure may restrict the tectonic processes which formed the AMR. Load emplacement on stronger older oceanic lithosphere can be eliminated for the AMR, as flexure of the lithosphere beneath the load of the ridge is not supported by this analysis. There is no evidence that the ridge is



regionally compensated, such as is the case for the Hawaii-Emperor Seamounts and the Western Walvis Ridge, where midplate volcanism occurred on old and strong lithosphere (Detrick and Watts, 1979). The inferred weakness of the lithosphere with the suggested density and thickness restricts the range of acceptable tectonic models.

#### **4.1 Near Spreading Center Hotspot Activity**

The inferred lithospheric weakness is incompatible with any tectonic model that proposes a long time separation between the formation of the underlying lithosphere and the eruption of volcanics to create the ridge. As previous studies have noted, the AMR has a similar crustal structure to other igneous aseismic oceanic plateaus, namely similar average density and thick crust (Jackson et al., 1986). These are characteristic of load emplacement on weak and young oceanic crust, such as in the case of near-spreading center hotspot activity as can be seen on the Eastern Walvis Ridge and the Ninety-East Ridge (Detrick and Watts, 1979). If the oceanic crust around the AMR formed very close to the time of ridge formation, it would be compatible with this result. Two plate boundary configurations in the Amerasian Basin could produce this environment.

First, this can be achieved by having the hotspot under the spreading center that rotationally opened the southern Canada Basin. This implies the hotspot would be stationary beneath the spreading axis so that the ends of the AMR formed first during the initiation of rifting (figure 4.1). It follows that the center is the youngest, forming at the end of spreading, so that all portions of the AMR formed near-ridge. This is not consistent with current evidence. The best age constraints for the AR come from fossils, which suggest formation in the late Cretaceous (Von Wagoner et al., 1986). The fossils were found close to the continental shelf, a location in this model where the ridge should be the oldest, with an age close to the time of the opening of the Canada Basin in Early Cretaceous around 135 Ma (Grantz et al., 1998). While it is possible that the age of the lower AR could be older (since the sedimentary evidence constrains youngest possible age), so that the Canada Basin and the AMR could have formed coincidentally, there is

also evidence that suggests the hotspot was beneath Ellesmere Island by around 92 Ma (Tarduno et al., 1998) on its path south towards Iceland. It is unlikely that in such a short timescale the hotspot jumped half way across the Arctic Ocean.

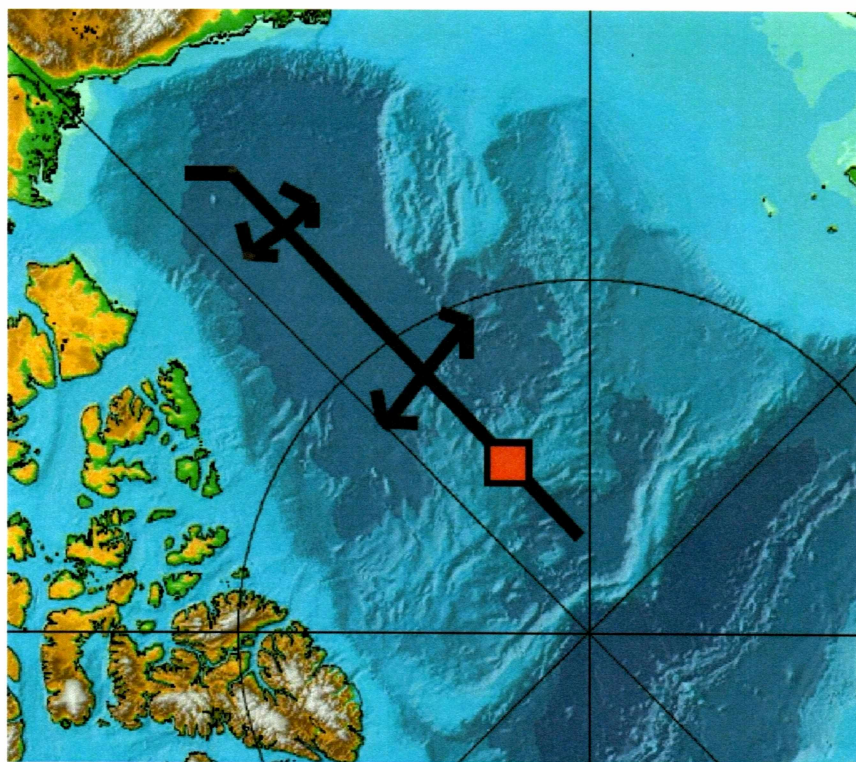


Figure 4.1: Geometry of first near-ridge hotspot model. Black line indicates location of hypothesized spreading axis, arrows show spreading direction. Hotspot location during time of spreading indicated by red box. This implies a long transform fault at the Lomonosov Ridge. Map source: Jakobsson et al. (2000).

Alternatively, since studies suggest the rotational spreading in the southern Canada Basin had ceased before the formation of the AMR (Grantz et al., 1998), a second stage of spreading could be required in the Late Cretaceous near the AMR, such as in the Makarov Basin or immediate area of the northern Canada Basin (figure 4.2). Various studies have suggested that the origin of the Makarov Basin is closely tied to the formation of the AMR, as they share very similar seismic structure (Jackson and Johnson, 1986) and magnetic anomalies. Magnetic anomaly maps (e.g. Glebovsky et al., 2000) show the AMR, immediate vicinity of the Canada Basin, and the Makarov Basin, as a

virtually indistinguishable magnetic muddle with very large magnitude anomalies, while all other basin areas, ridges, and margins of the Arctic are distinctly different with smoother low magnitude anomalies. Such a high magnitude magnetic muddle could be expected from an oceanic plateau near the area of spreading (Forsyth et al., 1986b) during the Cretaceous magnetic normal period between 120-80 Ma (Forsyth et al., 1986b). If there were spreading there during the Late Cretaceous with the Icelandic hotspot underneath, the AMR could form as a near-ridge hotspot plateau similar to the current system in Iceland. Seismic evidence over the adjacent Makarov Basin is consistent with that of oceanic crust that is thicker by the influence of nearby hotspot activity (Sorokin et al., 1999). Unfortunately the location of this second extinct spreading axis is not obvious. The AMR is bathymetrically too high to be a Cretaceous-aged spreading center, as was argued by Delaurier (1978). But, if the AMR were the result of hotspot activity funneling material into the spreading axis, it could trace the location of spreading while not satisfying the age-depth relationship for oceanic crust due to its thickened root. However, it is difficult to understand how a spreading axis as long as the AMR could have all been fed by the same hotspot during a period of 20-30 Myr. Spreading in the Makarov Basin or northern Canada basin on an axis parallel to the AMR also do not explain the formation of the AMR by near-ridge hotspot activity, as hotspot funneling would be expected to form plateaus symmetric about the ridge axis (Vink, 1984a).

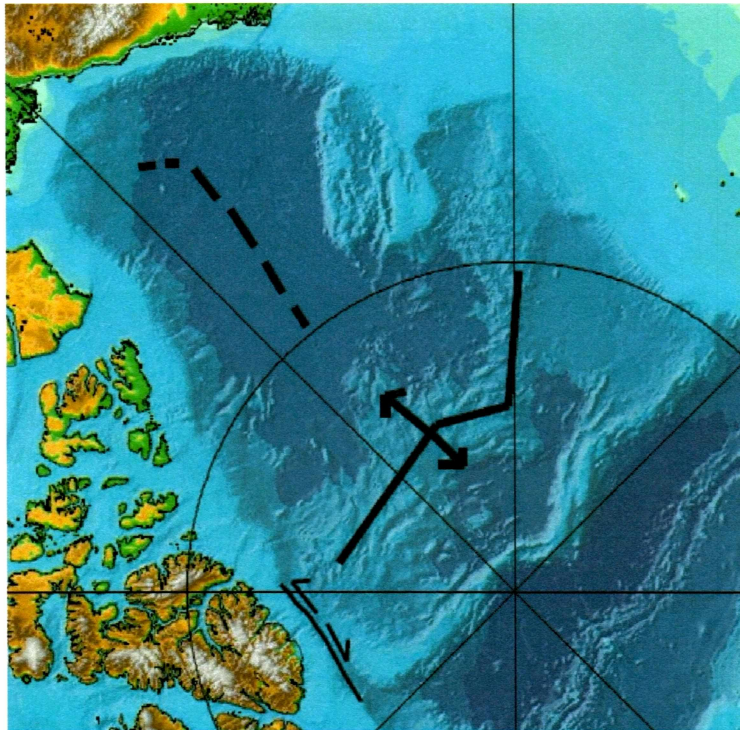


Figure 4.2: Geometry of second near-ridge hotspot model. The axis of the first stage of spreading in southern Canada Basin is indicated by the dashed line. Second stage of spreading near the AMR drawn on ridge axis, arrows indicate spreading axis parallel to the AMR. Model requires hotspot to feed entire second stage spreading axis, but location is unclear. Map source: Jakobsson et al. (2000).

In both configurations of spreading for the Amerasian Basin, there are problems due to age inconsistencies and geometry of the AMR formation. In addition, the near-ridge oceanic plateau model is not compatible with the geologic evidence which suggests the AR is a product of midplate volcanism (Von Wagoner et al., 1986), nor with the dredged limestones found on the MR (unpublished data from presentation by Kaban'kov et al., given in St Petersburg, 2003).

#### 4.2 Rifted Continental Fragment

Another tectonic model compatible with a weak lithosphere was presented by Miller et al. (2006), suggesting that the AMR rifted from the Lomonosov Ridge. Rifting within continental material is much more frequently observed than oceanic rifting, as

thick continental lithosphere is significantly weaker than its thin oceanic counterpart (Vink et al., 1984b). The new lithosphere forming in the rift axis is weak, as a result of complete loss of strength during rifting, so a rifted AMR would be expected to exhibit local isostasy. However, extremely thick sediment layers are characteristic of continental shelves, and current evidence suggests that the sediment layer over the AMR is 600 m to 1 km at its maximum (Jokat, 2003; Dove et al., 2006). This observed sedimentary layer is more typical of pelagic sediment deposition from mid-ocean environments rather than thicker sediments from close to the continents. Much of the sedimentary data on the AR also suggests that there was extensive volcanism during the Late Cretaceous (Clark, 1974), as do dredging results from the CESAR mission (Von Wagoner et al., 1986). This volcanism could be explained by passive upwelling, which is a source of midplate volcanism and could produce alkalic basalts like those dredged off the AR (Von Wagoner et al., 1986). This is also consistent with the seismic results over the AR which imply oceanic basement (Jokat, 2003). Rifting is also compatible with previous studies over the MR which dredged limestone and other rocks of continental origin (unpublished data from presentation by Kaban'kov et al., given in St Petersburg, 2003). Despite the argument that the high amplitude magnetic muddle is typical of oceanic plateaus made earlier in the discussion, this signature has also been suggested as evidence of its continental origin, as all other such high amplitude occurrences on earth are from continental crust (Coles and Taylor, 1990). If the AMR is a rifted continental fragment, it is reasonable to assume it rifted off the Lomonosov Ridge while it was still attached to the Barents Shelf (figure 4.3), perhaps explaining the kink that is mimicked in both ridges. In addition the AMR may have undergone extension after rifting, and this may explain why the AMR exhibits some graben-like bathymetric features. Rifting may have led to the development of seafloor spreading in the Makarov Basin. While the seismic study over the Makarov Basin has been interpreted as hotspot influenced oceanic crust, due to the sparse data, continental origin could not be ruled out (Sorokin et al., 1999). Although no convincing evidence of seafloor spreading there has been found, linear

magnetic anomalies would not be present if it formed during the Cretaceous magnetic normal period, as is thought to be the case.

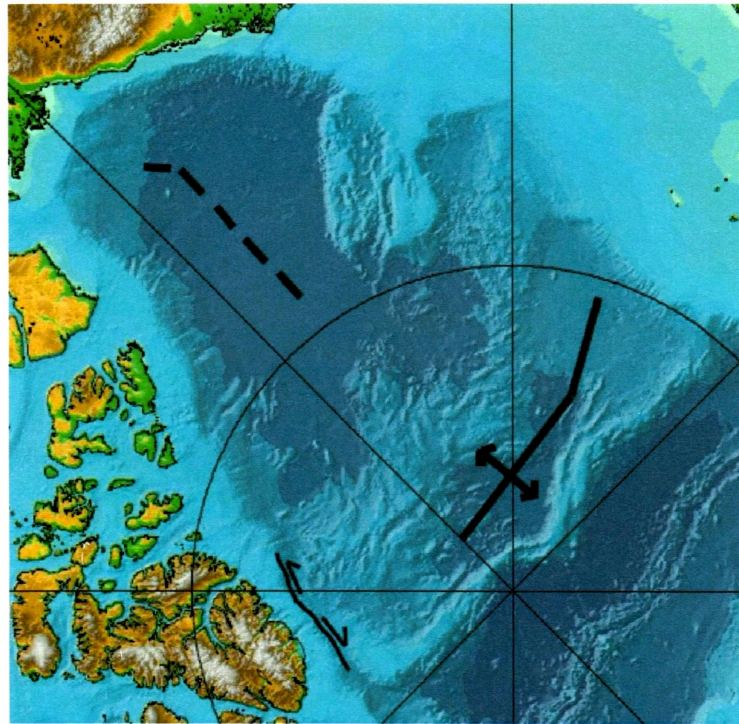


Figure 4.3: Geometry of the AMR as rifted continental margin. First stage of spreading in southern Canada Basin indicated by dashed line. Second stage of rifting and possibly spreading between the AMR and Barents Shelf (now Lomonosov Ridge) shown in solid black. Arrows indicate direction of spreading. Map source: Jakobsson et al. (2000).

### 4.3 Consistent Tectonic Models of the Amerasian Basin

All of these models of formation of the AMR have their own implications for the opening of the Amerasian Basin. The capture and isolation of part of the Kula plate in the Arctic can be eliminated by all of them, as this would require the AMR to be a product of midplate volcanism, or be of Jurassic age. Either of these conditions would infer a long time between crustal formation and ridge eruption, which would require a strong lithosphere. This would be inconsistent with the primary results of this study. While the inferred weak lithosphere further restricts the acceptable tectonic models for the basin,

none of the other three main classes of models discussed in the introduction can be completely ruled out.

The two near-ridge hotspot configurations discussed in section 4.1 each have separate implications. The first, which suggested that the hotspot was active beneath the spreading axis that formed the Canada Basin, is incompatible with the Arctic Canadian Transform model, as it relies on seafloor spreading perpendicular to the AMR axis all the way to the Lomonosov Ridge. This is the essence of the rotational model, however the Arctic Alaska Transform may also be consistent if the spreading axis was extended to the Lomonosov Ridge. The second near-ridge hotspot geometry allows for some expansion from the pure rotational model, because of the second stage of spreading in the AMR vicinity. This means during the course of the opening of the Amerasian Basin, there was a stage of spreading perpendicular to the AMR, followed by spreading parallel to the AMR (a combination of model classes). The AMR vicinity was thus formed by Arctic Canadian transform motion while the southern Canada Basin up to the AMR could have formed by either by rotation or Arctic Alaska transform spreading.

The continental rift model requires an Arctic Canadian Transform model, at least in part. Rifting or spreading in the Makarov Basin between the AMR and the Barents Shelf requires transform motion along the Arctic Canadian Islands, for at least the length between the Lomonosov Ridge and the AMR. For the Canada Basin the implication in this case is less clear, but it is likely that the rotational model would still hold south of the AMR. This is the arrangement suggested by Miller et al. (2006) to accommodate geochronology from circum-Arctic sediments.

## 5. CONCLUSIONS

From the results of this study, it can be concluded that the AMR is one ridge, of common origin. The spectral analysis combined with crustal modeling was successful for the shiptracks. The crustal structure can be described as a locally compensated ridge, with an average crustal density of  $2.75 \text{ g-cm}^{-3}$  and average crustal thickness of 30 km.

The ridge structure inferred from the shiptrack data is consistent with near-ridge hotspot activity, as well as that of rifted continental crust. But it is clear that in order to fully disclose the tectonic history of the AMR and the prevailing mystery as to its origin, more studies of the crustal structure of the AMR are needed. Seismic refraction and reflection exploration and scientific drilling are likely to be the most fruitful paths to take. Core drilling has never been done, and the only existing in situ samples were taken over the ridge by dredging. With the exception of these dredged samples we have no knowledge of the composition of the bedrock anywhere along the ridge. Unfortunately the isostatic study cannot distinguish between continental or oceanic composition. Drilling will be necessary to distinguish between a continental or oceanic crust. This distinction is one of the biggest missing pieces of evidence which would make it possible to understand the tectonic origin of this ridge. Only after we understand the origin of the AMR will we be able to discover the tectonic history of the Amerasian Basin.



## REFERENCES

- Arfken, G.B., and H.J. Weber, *Mathematical Methods for Physicists*, 1112 pp., Harcourt Academic Press, New York, NY, 2001.
- Asudeh, I., A.G. Green, D.A. Forsyth, Canadian expedition to study the Alpha Ridge complex: results of the seismic refraction survey, *Geophysical Journal*, *92*, 283-301, 1988.
- Belousov, V.V., Against the hypothesis of ocean-floor spreading, *Tectonophysics*, *9*, 489-511, 1970.
- Bevington, P.R., and D.K. Robinson, *Data Reduction and Error Analysis for the Physical Sciences*, 328 pp., McGraw-Hill, Inc., New York, NY, 1992.
- Blakely, R. *Potential Theory in Gravity and Magnetic Applications*, 441 pp., Cambridge University Press, New York, NY, 1996.
- Brozena, J.M., V.A. Childers, L.A. Lawver, L.M. Gahagan, R. Forsberg, J.I. Faleide, O. Eldholm, New aerogeophysical study of the Eurasia Basin and Lomonosov Ridge: Implications for basin development, *Geology*, *31*, 825-828, 2003.
- Childers, V.A., D.C. McAdoo, J.M. Brozena, S.W. Laxon, New gravity data in the Arctic Ocean: Comparison of airborne and ERS gravity, *Journal of Geophysical Research*, *106*, 8871-8886, 2001.
- Clark, D.L., Late Mesozoic and Early Cenozoic Sediment Cores from the Arctic Ocean, *Geology*, *2*, 41-44, 1974.
- Coakley, B.J., and J.R. Cochran, Gravity evidence of very thin crust at the Gakkel Ridge (Arctic Ocean), *Earth and Planetary Science Letters*, *162*, 81-96, 1998.
- Cochran, J.R., An Analysis of Isostasy in the World's Oceans 2: Midocean Ridge Crests, *Journal of Geophysical Research*, *84*, 4713-4729, 1979.
- Cochran, J.R., M.H. Edwards, B.J. Coakley, Morphology and structure of the Lomonosov Ridge, Arctic Ocean, *Geochemistry, Geophysics, Geosystems*, *7*, Q05019, 2005.
- Coles, R.L., and P.T. Taylor, Magnetic Anomalies, in *The Geology of North America*, vol. L, *The Arctic Ocean Region*, edited by A. Grantz, L. Johnson, J.F. Sweeney, pp. 119-132, Geological Society of America, Boulder, Colo., 1990.
- Cooley, J.W., and J.W. Tukey, An Algorithm for the Machine Calculation of Complex Fourier Series, *Mathematics of Computation*, *19*, 297-301, 1965.
- Crane, R.C., Arctic reconstruction from an Alaskan viewpoint, in *Alaskan North Slope Geology*, edited by Tailleux, I.L. and P. Weimer, pp. 769-784, Society of Economic Paleontologists and Mineralogists, Pacific Section, Special Publication 50, 1987.
- DeLaurier, J.M., The Alpha Ridge is not a spreading centre, *Publication of the Earth Physics Branch*, *45*, 87-90, 1978.
- Detrick, R.S., and A.B. Watts, An Analysis of Isostasy in the World's Oceans 3: Aseismic Ridges, *Journal of Geophysical Research*, *84*, 3637-3653, 1979.

- Dove, D., B.J. Coakley, J. Hopper, A geophysical survey of the Mendeleev Ridge; Processing steps and preliminary interpretations, *Geological Society of America Abstracts with Programs*, 38, 84, 2006.
- Edwards, M.H., and Coakley, B.J., SCICEX Investigations of the Arctic Ocean System, *Chem. Erde*, 63, 281-328, 2003.
- Embry, A.F., and J. Dixon, The Age of the Amerasia Basin, in *Proceedings of the 1992 International Conference on Arctic Marings*, pp. 289-295, US Mineral Management Service Report 94-0040, 1994.
- Embry, A.F., and Osadetz, K.G., Stratigraphy and tectonic significance of Cretaceous volcanism in the Queen Elizabeth Islands, Canadian Arctic Archipelago, *Canadian Journal of Earth Sciences*, 25, 1209-1219, 1988.
- Forsyth, D.A., I. Asudeh, A.G. Green, H.R. Jackson, Crustal structure of the northern Alpha Ridge beneath the Arctic Ocean, *Nature*, 322, 349-352, 1986a.
- Forsyth, D. A., P. Morel-A-L'Huissier, I. Asudeh, A.G. Green, Alpha Ridge and Iceland- Products of the same plume? *Journal of Geodynamics*, 6, 197-214, 1986b.
- Glebovsky, V.Y., L.C. Kovacs, S.P. Maschenkov, J.M. Brozena, Joint Compilation of Russian and US Navy Aeromagnetic Data in the Central Arctic Seas, *Polarforschung*, 68, 35-40, 2000.
- Grantz, A., D.L. Clark, R.L. Phillips, S.P. Srivastava, Phanerozoic stratigraphy of Northwind Ridge, magnetic anomalies in the Canada Basin, and the geometry and timing of rifting in the Amerasia Basin, Arctic Ocean, *GSA Bulletin*, 110, 801-820, 1998.
- Grantz, A., S.D. May, P.T. Taylor, L.A. Lawver, Canada Basin, in *The Geology of North America*, vol. L, *The Arctic Ocean Region*, edited by A. Grantz, L. Johnson, J.F. Sweeney, pp. 379-402, Geological Society of America, Boulder, Colo., 1990.
- Halgedahl, S.L., R.D. Jarrard, Paleomagnetism of the Kuparuk River formation from oriented drill core: evidence for rotation of the Arctic Alaska plate, in *Alaskan North Slope Geology*, vol. 2, edited by I. Tailleux, P. Weimer, pp. 581-617, Pacific Section, Society of Economic Paleontologists and Mineralogists, 1987.
- Hall, J.K. Arctic Ocean Geophysical Studies: The Alpha Cordillera and Mendeleev Ridge, in Office of Naval Research Technical Report CU-2-70, 125 pp., Washington, DC, 1970.
- Hall, J.K., Geophysical Evidence for Ancient Sea-floor Spreading from Alpha Cordillera and Mendeleev Ridge, in *Arctic Geology*, vol. 19, pp. 542-561, edited by M.G. Pitcher, American Association of Petroleum Geologists, Memoir, 1973.
- Herron, E.M., J.F. Dewey, W.C. Pitman, Plate Tectonics Model for the Evolution of the Arctic, *Geology*, 2, 377-380, 1974.
- Jackson H.R., and G.L. Johnson, Summary of Arctic Geophysics, *Journal of Geodynamics*, 6, 245-262, 1986.
- Jackson, H.R., D.A. Forsyth, G.L. Johnson, Oceanic affinities of the Alpha Ridge, *Marine Geology*, 73, 237-261, 1986.
- Jackson, H.R., A. Grantz, I. Reid, S.D. May, P.E. Hart, Observations of anomalous oceanic crust in the Canada Basin, Arctic Ocean, *Earth and Planetary Science Letters*, 134, 99-106, 1995.